scientific reports

Check for updates

OPEN

Developmental differentiation of mouse inner ear neuron subpopulations resolved with a peripherin-promoter reporter within the *Grm8* locus

Lily J. Pearson[1], Jeremy L. Pinyon[1,6], Jennie M. E. Cederholm[1], Georg von Jonquieres[1], Florence Bartlett[2], Xabier Vázquez-Campos[3], Fabien Delerue[4], Lars M. Ittner[5] & Gary D. Housley[1]✉

Molecular profiling of inner ear neurons has broadened the classification of the primary afferents that support neural coding for hearing and balance. To extend spatiotemporal characterization of auditory and vestibular neuron diversity, we established a transgenic reporter mouse model (*Prph*$_p$-mCherry), where elements of the peripherin promoter (*Prph*$_p$) drive expression of the mCherry fluorescent reporter. Type III intermediate filament protein peripherin expression is a marker for type II spiral ganglion neurons (SGN) that innervate the cochlear outer hair cells, and the small diameter 'bouton' vestibular ganglion neurons (VGN) innervating the type II vestibular hair cells. Using Nanopore genome sequencing, the integration site of the transgene construct was identified within the class III metabotropic glutamate receptor 8 gene (*Grm8*, chromosome 6). Use of CUBIC / PEGASOS clearing of early postnatal to adult inner ear tissues enabled *in situ* 3D spatial localization of a dispersed population of cochlear mCherry + ve SGN, with highest expression and density in the hook (high frequency encoding) basal region. Of these mCherry + ve SGN, type II SGN (peripherin-immunopositive) were all co-labeled in the basal region, but the majority of the overall mCherry-delineated SGN auditory subpopulation were type I SGN innervating inner hair cells. In the VGN, mCherry + ve neurons represented ~ 15% of the adult population, dispersed as a small diameter subpopulation throughout both the inferior and superior VGN regions. These findings resolve heterogeneous type I and type II cochlear SGN subpopulations, particularly in the structurally complex hook region, and further differentiate vestibular primary afferents across postnatal development.

Abbreviations

ABR	Auditory Brainstem Response
AC	Anterior canal
BGHpA	Bovine growth hormone
CUBIC	Clear unobstructed brain imaging cocktails and computational analysis
dB SPL	Decibels Sound Pressure Level
DPOAE	Distortion Product Otoacoustic Emissions
GGN	Geniculate ganglion neurons
hDTR	Human diphtheria toxin receptor
IHC	Inner hair cell
INF	Inferior

[1]Translational Neuroscience Facility, Department of Physiology, School of Biomedical Sciences, UNSW, Sydney, NSW, Australia. [2]KGLMF Mark Wainwright Analytical Centre, UNSW, Sydney, NSW, Australia. [3]School of Biotechnology and Biomolecular Sciences, UNSW, Sydney, NSW, Australia. [4]Department of Genetics, The University of Texas MD Anderson Cancer Center, Houston, TX, USA. [5]Faculty of Medicine, Health and Human Sciences, Department of Biomedical Sciences, Dementia Research Centre, Macquarie University, Sydney, NSW, Australia. [6]Discipline of Physiology, School of Medical Sciences, Charles Perkins Centre, University of Sydney, Camperdown, NSW, Australia. ✉email: g.housley@unsw.edu.au

IRES	Internal ribosome entry site
LC	Lateral canal
OHC	Outer hair cell
OSL	Osseous spiral lamina
PC	Posterior canal
PEGASOS	Polyethylene glycol-associated solvent system
pLDDT	Predicted local distance difference test
RC	Rosenthal's canal
ROI	Region of interest
SA	Saccule
SGN	Spiral ganglion neurons
SUP	Superior
UT	Utricle
UTR	Untranslated region
VFT	Venus fly trap
VGN	Vestibular ganglion neurons
WPRE	Woodchuck hepatitis virus posttranscriptional regulatory elements
WT	Wildtype

Inner ear primary afferent neurons lie within the cochlear spiral ganglion and the vestibular (Scarpa's) ganglion, with neurite projections to sensory hair cells encoding sound and balance. A diversity in characteristics is recognized by subtype classifications of these afferents, where multiomics and transgenic models are delineating heterogeneity.

Spiral ganglion neurons (SGN) are structurally defined by their hair cell connectivity in the early postnatal period[1]. Type I SGN represent ~ 95% of the primary auditory afferent neurons and tens of type I SGN form exclusive single synapse innervation with each inner hair cell (IHC), to achieve precise tonotopically mapped sound coding. Within the small subpopulation of type II SGN each SGN innervates multiple outer hair cells (OHC)[2,3]. The physiological significance of the type II SGN afferents remains controversial[4], where proposed roles include potential activation by damaging noise levels and 'nociceptive' pain[5,6]. There is also consolidation of evidence that the type II SGN contribute to the sensory drive to the efferent feedback control of the cochlear amplifier[7–9]. Subtypes of type I SGN afferents exhibit distinct electrophysiological characteristics, alongside specific variations in synapse placement on individual IHC. Modiolar-oriented IHC synapses exhibit low spontaneous firing rate (high threshold and dynamic range), while afferents synapsing with the pillar face exhibit high spontaneous rates (low threshold) and limited dynamic range[10]. It is likely that the dynamic range supporting hearing comprehension relies on the parallel coding from these multiple afferent connections with IHC[11].

Single cell transcriptomics has been used to parse type I SGN into three molecularly distinct subtypes (type Ia, Ib and Ic). Based on a distinct mRNA transcript profile, the pillar-facing high spontaneous rate SGN are now classified as type Ia, with modiolar-oriented SGN defined as Ib and Ic subtypes[12–14]. SGN sampling along the length of the cochlea indicates broad retention of these subpopulations with cochlear tonotopicity, albeit with some evidence for changes in subtype proportion, where for example, type Ic SGN representation increases in the basal (high frequency – encoding) region[15].

The vestibular (Scarpa's) ganglion comprises primary afferent neurons innervating the otolith organs (utricle and saccule) and the semicircular canal ampullae. These organs initiate signals needed for balance, and compensatory movement of the eyes, head and neck[16,17]. Vestibular ganglion neurons are also categorized by their connectivity to their mechanosensitive hair cells, with type I vestibular hair cells synapsing with large diameter calyx afferents and type II vestibular hair cells synapsing with small diameter bouton afferents[18]. Many vestibular neurons show dimorphic properties branching to synapse with both type I and type II hair cells of the maculae of the otolith organs and semicircular canal cristae[19–21]. Bouton vestibular afferent fibers are known to express the type III intermediate filament peripherin[22], which is also a type-marker for the cochlear type II SGN[23–26], confirmed by RNAseq [12,13].

Localization and dissection of functional elements of the gene sequence encoding peripherin have been utilized to pursue authentic models of peripherin expression in peripheral and central neuronal populations in transgenic mice[27]. In addition to the peripherin promotor region, upstream and intragenic regions are required for cell-type specific expression in the hind brain and dorsal root ganglion[18,28–33]. Given the consensus for using the peripherin mRNA transcript as a primary molecular marker for type II SGN[11–13,15,34] and this expanded peripherin promotor domain ($Prph_p$), the present study established a peripherin reporter transgenic mouse directed to extend the spatiotemporal characterization of spiral and vestibular ganglion neuron diversity across postnatal development of the inner ear. In combination with integration of the mCherry reporter transgene within *Grm8*, the class III metabotropic glutamate receptor gene (type Ic SGN marker), new populations of inner ear primary afferents are resolved using 3D *in situ* Lightsheet imaging.

Methods

The study followed the National Health and Medical Research Council Australian Code for the care and use of animals for scientific purposes[35]. The animal study design and protocols reflect the ARRIVE guidelines[36] and were approved by the UNSW Animal Care and Ethics Committee. All methods were performed in accordance with these guidelines and regulations. Mice used in these studies were euthanized by intraperitoneal injection of pentobarbital (Lethabarb,100 mg/kg, 100 mg/ml in normal Saline) using a 27 G needle; confirmed by absence of breathing and heart beat.

Prph$_p$- mCherry transgenic reporter mouse model

The *Prph*$_p$-mCherry transgene promoter included P1 / P2 peripherin promotor / repressor elements[29] and elements of the chicken β-actin (CBA) exon 1, 2, including the intron. The mCherry fluorescent reporter gene was downstream of a human Diphtheria Toxin Receptor (hDTR) element linked by an internal ribosome entry site (IRES); included for future functional studies. Woodchuck Hepatitis Virus Posttranscriptional Regulatory Element (WPRE) and bovine growth hormone (BGHpA) signal elements completed the 3' sequence. The 10,147 bp *Prph*$_p$-mCherry expression cassette is shown schematically in Fig. 1A. Microinjection of the linearized plasmid *Prph*$_p$-mCherry transgene into the pronucleus of mouse zygotes (Supplementary Fig. 1) following our established procedure[37] resulted in stable integration in ten founders, as detected by PCR using transgene specific primers. Genotyping was undertaken on DNA isolated from the tail tips using 25 µL PCR reactions, with primers targeting the hDTR and IRES regions (Forward primer: 5'-GAAAATGAAGAGAAAGTGAAGTTGG-3', Reverse primer 5'-CAAAAGACGGCAATATGGTGG-3', 159 bp amplicon) (Fig. 1B). We selected four lines that exhibited mCherry expression in the dorsal root ganglion, as a primary match to a peripherin phenotype (Fig. 1C). Of these four lines, only one (Line 43) showed strong cell-type specific expression in the inner ear SGN and VGN. This study reports the characterization patterns of transgene expression in this line. The line was backcrossed for five generations into the C57Bl/6J strain, and the homozygous mice used for this study reflect generations f14 – f18.

Determination of *Prph*$_p$-mCherry transgene integration site

The characterization of the *Prph*$_p$-mCherry transgene integration site was undertaken using PrometheION deep sequencing (Oxford Nanopore Technologies). The genomic DNA was obtained from a liver sample of a 10-week-old female transgenic mouse (Line 43), snap frozen in liquid nitrogen and homogenized with a mortar and pestle. The DNeasy blood and tissue midi kit (Qiagen; 13343) was used to extract and purify high molecular weight DNA (following manufacturer's instructions). A total of 3 µg of DNA was used with the Oxford Nanopore Technologies ligation sequencing kit v14 (chemistry LSK114). The elution time at the end repair Ampure bead

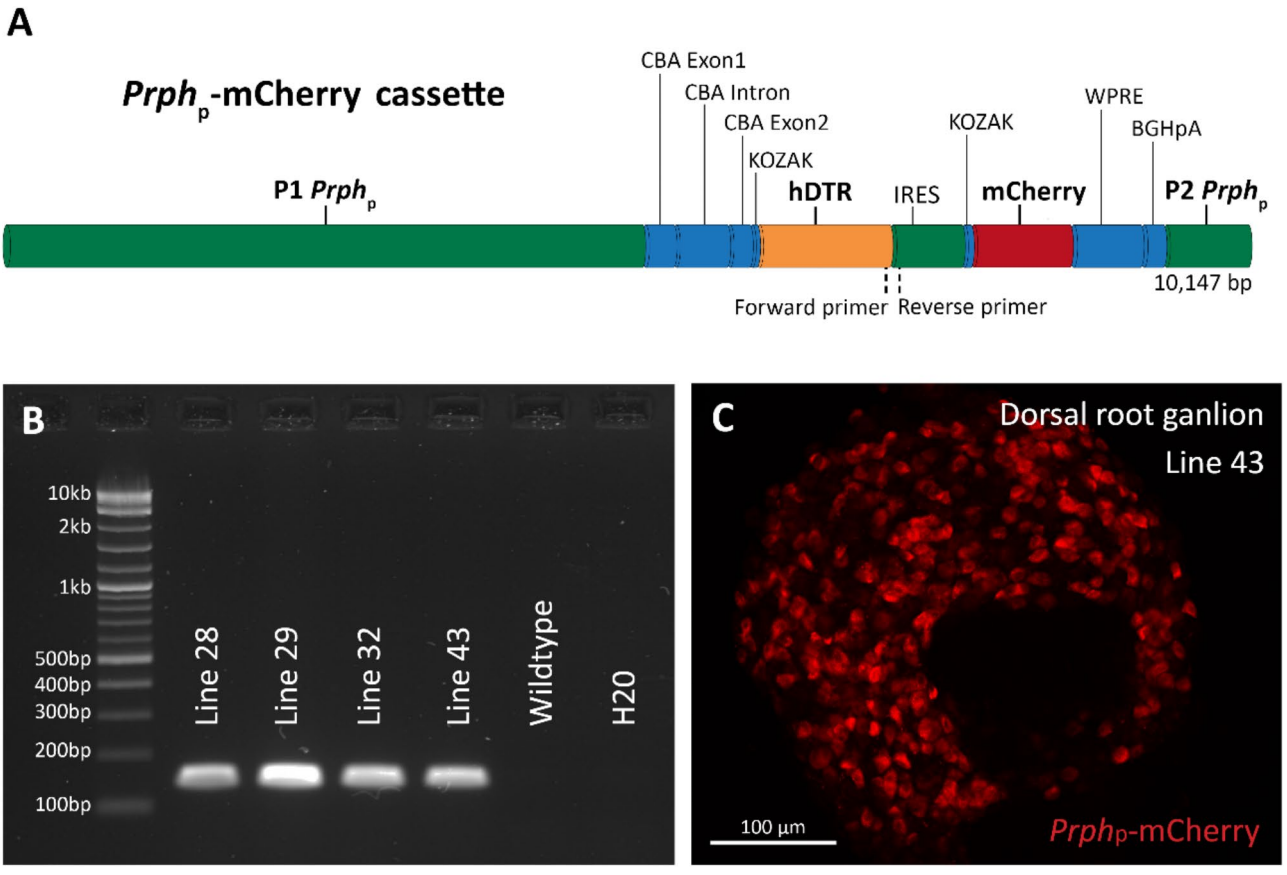

Fig. 1. *Prph* promoter (*Prph*$_p$) driven - mCherry transgene cassette design and creation of mouse lines. (**A**) The mCherry reporter is flanked by an upstream P1 *Prph*$_p$ element and a downstream P2 *Prph*$_p$ repressor element[29]. The construct included the CBA (Chicken β-actin) promoter, KOZAK sequences, the human Diphtheria Toxin Receptor (hDTR) coding sequence element, expression regulatory domains and regulatory sequences including: CBA exon 1, 2, CBA intron, KOZAK sequences, IRES (internal ribosome entry site), WHP (Woodchuck Hepatitis Virus), WPRE (Posttranscriptional Regulatory Element), BGHpA (bovine growth hormone poly A). (**B**) PCR genotyping of the transgene as shown in (**A**) exhibited mCherry expression in the dorsal root ganglion (shown for Line 43 in **C**).

clean-up was set to 10 min. Long fragment buffer was used in the final Ampure bead clean-up and the elution step took 30 min at 37 °C. Sequencing was performed on the Oxford Nanopore PromethION platform using a version R10.4.1 flow cell. Base calling was performed with Guppy v6.5.7 + ca6d6afd options --calib_detect --trim_adapters --do_read_splitting --detect_mid_strand_adapter[38] and the super accuracy model. Raw sequencing data have been deposited in the European Nucleotide Archive (ENA) under project PRJEB79255.

As initial attempts were unsuccessful in locating the site of the inserted transgene with structural variant pipeline analysis algorithms (e.g. Sniffles2), a *de novo* whole genome assembly was performed with Raven v1.8.1[39,40]. Promoters and genes from the construct were identified against the Raven assembler to locate the insertion site. The contig with the insert was then mapped against the Ensembl 109 Mus musculus primary assembly (GRCm39) in D-GENIES[41]. A region of interest (ROI) of 2 Mbp about the insert, corresponding to chr6:27,000,000–29,000,000 in the reference genome (which includes the metabotropic *Grm8* gene) was defined for reassembly. Reads mapping to the ROI with minimap2 v2.26 were reassembled multiple times to solve the complexity of the graph assembly around the insertion site[42]. Finally, manual tuning of the graph assembly from a read subset assembled with Flye v2.9.2-b1786 and standard parameters[43], produced an assembly satisfying all observations. The final ROI assembly was polished with Racon v1.5.0[44] and the annotations from the reference genome transferred to it with Liftoff v1.6.3[45]. The annotated ROI for the integrated $Prph_p$-mCherry transgene within *Grm*8 locus of the mouse (Line 43) genome is publicly available in ENA under project PRJEB79255.

Hypothetical resulting proteins as well as their native counterparts were modelled as homodimers as implemented in Colabfold v1.5.2[46] with options --stop-at-score 95 --recycle-early-stop-tolerance 0.5 --amber --use-gpu-relax.

Immunofluorescence

Extraction and preparation of mouse inner ear tissue

Tissue was collected from mice at developmental timepoints from postnatal day 1 (P1) to adult (10–16 weeks). Mice older than P14 underwent cardiac perfusions, while P1 and P7 had their cochleae removed and perfused directly through the round window (scali perfusion). Cardiac perfusions were performed with a 10 ml flush of 0.1 M phosphate buffered saline (PBS, pH 7.6) followed by 10 ml 4% paraformaldehyde (PFA in 0.1 M PBS, pH 7.2). The inner ear was dissected and post-fixed overnight, then transferred to PBS. Inner ears were decalcified in 8% EDTA (0.1 M PBS, pH 7.8, Sigma-Aldrich; E5134) on a rotator at 4 °C for 5–7 days and then washed with PBS. For immunofluorescence, intact samples were further processed for clearing and Lightsheet imaging or sectioned for confocal imaging.

CUBIC / PEGASOS inner ear clearing and Immunolabeling

CUBIC (clear, unobstructed brain imaging cocktails and computational analysis) and PEGASOS (Polyethylene glycol-associated solvent system) solutions designed previously were combined in this method to visualize the entirety of the neuronal populations inside the cochlea structure[47,48]. Whole inner ear samples were cleared with a process outlined in Fig. 2A and Supplementary Table (1). The 'CUBIC1' protocol proceeded across 5–7 days, with solution changes every 2 days before washing three times for 6 h in PBS[48]. CUBIC1 is a water based solution made with 25% N, N,N',N'-tetrakis (2-hydroxypropyl)ethylenediamine (Sigma-Aldrich; 122262), 25% urea (Sigma-Aldrich, U5378-500G) and 15% Triton-X100 (Sigma-Aldrich; X100-100ML). The primary and secondary antibodies used in this study are listed in Supplementary Table (2). Antibodies were incubated for 5 days in a carrier solution containing serum (10% normal goat serum for TUBB3 (β3-tubulin) antibody, 5% normal donkey serum for Prph antibody) and 0.2% sodium azide in PBS. After the primary and secondary incubations, samples were left to wash in 0.1% Triton-X100 in PBS for 7 days on a rocker at room temperature.

After labeling, cochleae samples underwent PEGASOS dehydration, delipidation and refractive index matching protocol[47]. All PEGASOS solutions contained 3% N, N,N',N'-tetrakis(2-hydroxypropyl) ethylenediamine (Sigma-Aldrich; 122262). PEGASOS uses a 30–70% *tert*-butanol graded dehydration series (Sigma-Aldrich; 471712) followed by tB-PEG delipidation made with 70% *tert*-butanol and 30% PEG-MMA500 (Sigma-Aldrich; 447943). BB-PEG refractive index matching solution was made with 70% benzyl benzoate (Sigma-Aldrich; B6630) and 27% PEG-MMA500 as above.

Lightsheet in situ 3D image acquisition, pre-processing, segmentation and cell counting for whole samples

The benzyl-benzoate polyethylene glycol (BB-PEG) cleared inner ear tissue was mounted on the tip of a capillary, and data was acquired using a Lightsheet Z1 microscope (Zeiss) with Zen Black software (Version SP1, 2014; Zeiss). Excitation lasers (488 nm and 561 nm) were used with a 5x focusable objective for illumination (NA 0.1; nd 1.33–1.58) and a 5x collection objective (Plan Neofluar; NA 0.16; nd 1.33–1.56). The emission filters (488 nm: BP 505–545; 561 nm: BP575-615; Dichroic: 560) and laser power settings (488 nm: 29.5%; 561 nm: 30%) and exposure times (488 nm: 30 ms; 561 nm: 112.4 ms) were used for all images. Images were taken with an orientation to avoid variations caused by the elongated distortion in the z dimension; they were rotated until the cochlear "hook" region was a triangular shape and the vestibular ganglion structure was showing the highest surface area possible in a single plane. Dual-side illumination non-fused images were acquired, with the clearest side and least striping artifacts used to view the hook region and vestibular ganglion neurons (camera frame size: 1920 × 1920).

Channels were aligned with the Imaris (Version 9.9; Oxford Instruments) channel alignment tool, starting with z-plane alignment. The Imaris spot creation pipeline was used to identify and count single neurons for mCherry and Prph (Fig. 2B). The estimated diameter was set to 9.1 µm. Although acquisition settings were not modified between samples, processing thresholds varied as there were large baseline differences in intensity of the lowest intensity neurons across ages. Therefore, the recognition of each spot was checked manually and

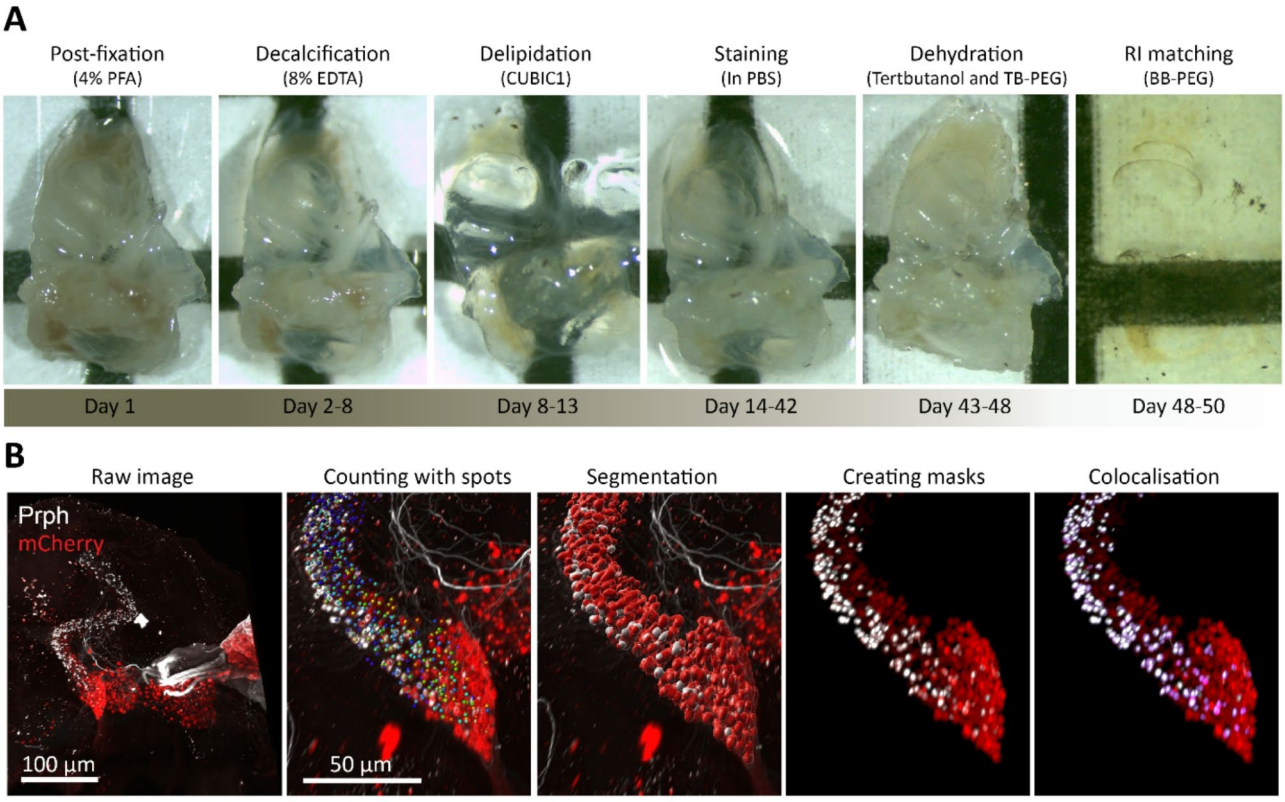

Fig. 2. CUBIC/PEGASOS clearing and processing of mouse inner ear - whole sample workflow. (**A**) Transparency of the sample during different stages of clearing, with the effect of each solution change visualized[47,48]. (**B**) Processing pipeline for samples imaged with the Zeiss Lightsheet Z1 microscope and analyzed in Imaris, from raw anti-mCherry (red) and anti-peripherin (white) *in situ* immunofluorescence through segmented analysis. Masks are established in the mCherry and Prph channels to identify cell bodies for generation of a colocalized channel (purple). Neuron counting (colored spots) occurs before clean-up and segmentation is used to create masks to further enable quantification of cell features.

in reference to a wildtype (WT) tissue sample. Spots recognizing non-specific puncta outside the spiral or vestibular ganglion were manually deleted. To assess Prph/mCherry colocalization, surfaces (3D mask) were generated to isolate positive SGN. The colocalization tool in Imaris was used to compare these surfaces; all data from the surfaces was selected to be included in the colocalization analysis. The images presented have undergone processing steps to remove non-specific or 'not of interest' structure of the inner ear. Non-specific removal of puncta includes small specks of antibody residing outside the spiral and vestibular ganglia and not of interest structures include fiber bundles attached to the outside of the inner ear bony structure. These clean-up steps were only performed on samples used in figures to facilitate visualization and colocalization analysis; clean-up processing occurred after cell counts.

Confocal Immunofluorescence imaging on cryosections

Cochlea tissue was cryoprotected with 10% sucrose (in milli Q water) overnight, then transferred to 30% sucrose overnight. Cryosectioning was performed with a Leica CM1850 cryostat. A cryomold (10 × 10 × 5 mm, Tissue Tech, USA) was filled with optimal cutting temperature compound (OCT) (Tissue Tech, USA). Sections were cut at 40 µm and transferred to wells (PBS). The floating sections were permeabilized and blocked for 2 h at room temperature using 10% normal goat serum (NGS; for samples processes with TUBB3 primary antibodies) or 5% normal donkey serum (NDS; for the Prph antibodies) and 1% TritonX-100 in PBS. The sections were sequentially incubated over night at 4 °C, in primary and then secondary antibodies (concentrations as described in Supplementary Table 2). Sections were incubated in appropriate serum with 0.1% TritonX-100 in PBS with 3× washing (10, 30 and 60 min) in 1 ml 0.1% TritonX-100 in PBS, then mounted on glass microscope slides (Livingstone, Australia) with ProLong® Gold Antifade with DAPI Molecular probes (Cell Signalling technology, USA). The methods of cryosection tissue collection, processing and immunohistochemistry were adapted from[8]. Images were acquired on a Zeiss LSM710 confocal microscope using Zen acquisition and analysis software (2014). The same acquisition parameters (pinhole size, pixel dwell time, laser power, zoom) were used for each type of image to ensure consistent sampling.

In each section, SGN were classified as apical – mid, basal and hook regions. The apical-mid region was defined as the SGN in Rosenthal's canal in the apical turn. The basal region was defined as turn 2 and the hook region was differentiated from the basal region on the basis of axial orientation, minimal osseous spiral lamina

structure and SGN axons projecting prominently basally. Cells were counted using ImageJ (Wayne Rasband, NIH; 1.53e). For each mCherry + ve cell, the area and mean pixel intensity in fluorescent arbitrary units (FAU) was recorded using the ImageJ oval shape selection tool. This was compared to the mean intensity for the same area on the TUBB3 channel. If the pixel intensity of mCherry cells were under 30 FAU, the cells were excluded from the cell count dataset, reflecting autofluorescence (based on WT baseline fluorescence). TUBB3 cells under 40 FAU were considered negative. Cells that were positive for mCherry, but negative for TUBB3, were added to the TUBB3 cell count to make the overall cell count.

Hearing testing

Testing was undertaken in a sound-attenuating chamber (Sonora Technology, Japan). BioSig32 software and an Auditory Brainstem Response (ABR) and Distortion Product Otoacoustic Emission (DPOAE) workstation (Tucker Davis Technologies system 3 with withRX6 and RX6-2 signal processors, USA) were used to capture test results (Fig. 12). A one-quarter-inch free field calibration microphone (model 7016, ACO, Japan) and BioSigRP software were used to calibrate the electrostatic speakers (TDT EC1) for each of the 5 sessions. *Prph*$_p$-mCherry and wildtype (WT) mice were anesthetized under 4% isoflurane on oxygen, followed by maintenance using 1–2%. Eye ointment was applied, and temperature regulated using a heat pad controlled via a rectal probe (Kent Scientific PhysioSuite). Subdermal platinum needle electrodes were inserted, with the ground electrode on right hind flank, the positive electrode inserted at the vertex and the negative electrode over the mastoid process. The speaker probe was inserted into the right ear canal[49]. ABR thresholds (dB SPL) were found for each click and pure tone stimulus frequency (4, 8, 16, 24 and 32 kHz). Each click and pure tone was delivered at 10 ms duration with broadband click of 100 µs, 10/s, in 5 ms tone pips, with a 0.5 ms rise/fall time. SPLs decreased in 5 dB steps from 70 dB SPL to 15 dB SPL below threshold (e.g. three waveforms with no observable ABR above the 100 nV noise floor). 512 ABR traces were averaged for each sound level.

The cubic ($2f_1–f_2$) DPOAE tests were conducted using an ER-B10 + microphone (Etymotic Research, USA) coupled to two EC1 speakers. The paired primary driver tones (168 ms duration; equal amplitude) were increased in 5 dB SPL steps from 0 to 70 dB SPL. DPOAE (fast Fourier transform), averaged for 50 repeats to establish thresholds (about 8, 12, 16, 24 and 32 kHz; where $f_2/f_1 = 1.2$). The threshold was defined as an amplitude of 5 dB above the noise floor, with the noise floor defined as an average of two peaks on either side of the DPOAE[49,50].

Statistics

Data were presented as mean ± standard error of the mean (s.e.m.). Statistical comparisons utilized $\alpha = 0.05$ to determine significance. Using Sigmaplot software (v.14, SysStat, Germany), group data were assessed for normal distribution and underwent parametric testing using t-test and ANOVA, including Holm-Sidak multiple pairwise *post-hoc* comparisons. Data which were not normally distributed were transformed for comparison (ranked sign test and ranked ANOVA). Data were analyzed for statistical outliers using the Grubb's test (extreme studentized deviate; PRISM). Graphical representation of data was undertaken using PRISM (Graphpad; Version 10; 2023). To establish the colocalization of peripherin and mCherry + ve neurons throughout development, a whole population counts for at least 3 biological repeats for each time point were compared with a two-way ANOVA with multiple comparisons. The difference between the proportion of mCherry cells in each region and across developmental timepoints was assessed using a one-way ANOVA pairwise multiple comparison. For whole SGN and VGN population counts from the 3D in situ visualization data, one-way ANOVA with multiple comparisons were used.

Results

Prph$_p$-mCherry transgene integration – associated *Grm8* exon reshuffling

PromethION Oxford Nanopore Technologies whole genome deep sequencing analysis of mouse Line 43 showed that two full copies of the *Prph*$_p$-mCherry transgene were integrated within the *Grm8* open reading frame on chromosome 6, 4427 bp from the intact 5' untranslated region (UTR), flanked by elements of a third copy (Fig. 3). The disruption to the *Grm8* locus included loss of exons 1 and 5, and duplication of exons 2, 3 and 4. Two exons disrupted the glutamate binding region (Venus's fly trap domain (VFT)). This reconfiguration includes a frame shift resulting in loss of the initial 279 amino acids (aa), an alignment between aa p.M280 and p.G386, and then alignment from p.G453 (NCBI BLAST, Supplementary Fig. 3, comparing the mouse native mGluR8 (accession no. NP_001298001.1 and mutant). In mouse, the VFT glutamate binding sites for mGluR8 are aa 156, 177–179, 227, 309 and 401 (by similarity; UniProt: P47743; GRM8_MOUSE) and while the latter two binding sites are retained, the translocation impacted the topology. Exons in the transmembrane and C-terminal domains are retained.

Comparison of native and transgene-modified mGluR8 protein structures

Using Alphafold2[51] protein structure modelling with AlphaFold-Multimer v3[52], the proposed mutant mGluR8 dimer structure resulting from transgene integration was compared with the native protein (Fig. 4). The confidence of this modelling was high, as shown by the predicted local distance difference test (pLDDT) (Supplementary Fig. 2). This modelling demonstrated loss of the N-terminal structure, including the critical VFT glutamate binding domain and associated dimer interaction sites, while the transmembrane domain elements and C-terminus regions appear normal. This *in silico* analysis, particularly the evident disruption of the glutamate binding domain, suggests that even with potential anomalous transcriptional activity, the Line 43 mouse is most likely to be a functional *Grm8* null.

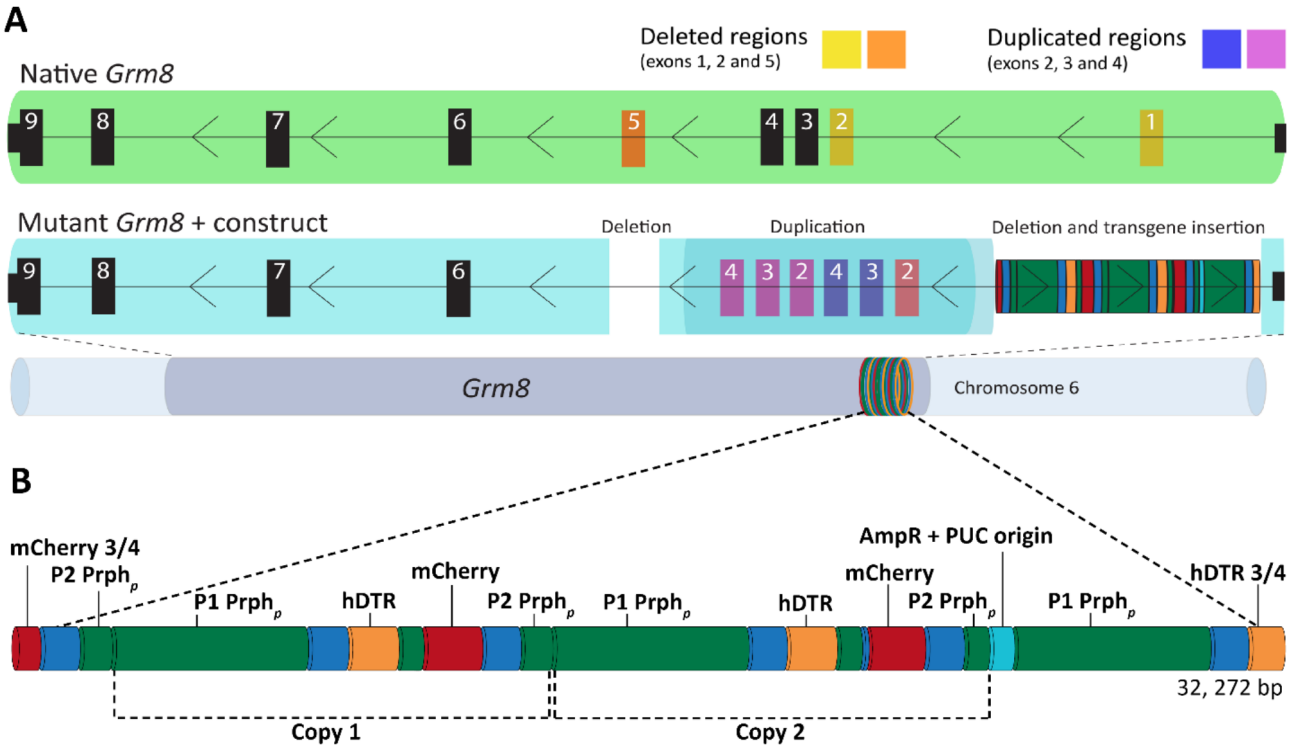

Fig. 3. *Prph*$_p$-mCherry transgene integration inside *Grm8* on chromosome 6. (**A**) Schematic of the integration of the *Prph*$_p$-mCherry transgene within the *Grm8* gene. The mutant *Grm8* disrupted by *Prph*$_p$-mCherry shows 2½ copies of the transgenic construct integrated 4 kb from the N-terminus coding region of *Grm8*. The black arrows indicate the direction of the reading frame, *Grm8* is transcribed right to left, while the transgene is transcribed left to right. Within the *Grm8* gene, 200 kb were deleted by the transgene integration, resulting in the deletion of exon 1 (yellow). This disruption extended into exon 2. Downstream exon 5 was also deleted (orange). Duplications of exons 2, 3 and 4 (pink) are noted. This schematic is modelled on the *Grm8* 201 isoform; given the *Prph*$_p$-mCherry transgene integration in the *Grm8* N-terminus region, alternative splicing of *Grm8* isoforms, which are clustered in the C-terminus, have no bearing on the mutated protein structure. (**B**) The transgene is concatenated and includes two full copies. The contig size is 1,830,475 bp, derived from Oxford Nanopore Technologies sequencing.

Overview of Prph$_p$-mCherry transgene expression in the adult cochlea and vestibular systems

In situ visualization of the intact inner ear of adult *Prph*$_p$-mCherry transgenic mice revealed populations of mCherry immunopositive neurons within the spiral and vestibular ganglia (Fig. 5). In the cochlea, a distinct population of mCherry + ve SGN resided in the hook region (encoding the highest sound frequencies), with a rapidly diminishing gradient of reporter expression towards the mid-cochlear level. This tissue was co-immunolabeled for the type III intermediate filament peripherin, a marker for the cochlear type II SGN, the anticipated target for the *Prph*$_p$ promoter-driven - mCherry reporter expression. There was a substantial mismatch between the reporter and peripherin labeling, given the basal region bias to the mCherry + ve SGN distribution, while the type II SGN population was broadly distributed throughout Rosenthal's canal. Both the afferent neurite projections to the cochlear hair cells and the central axon projections were unlabeled for the mCherry reporter, but the type II SGN neurites and axons exhibited peripherin immunolabeling.

In the vestibular ganglion (encompassing the afferents for the labyrinth and otolith end-organs), the expression of mCherry + ve neurons was biased towards the smaller diameter somata across both the superior and inferior regions. In contrast to SGN, the VGN somata lacked peripherin immunolabeling, but peripherin + ve nerve fibers (bouton afferents) branched to the semicircular canals and otolith organs.

Developmental regulation of Prph$_p$-mCherry transgene - delineated inner ear neurons

While the basal spatial compartmentalization of mCherry + ve SGN was evident at birth, the population varied considerably with postnatal development (Fig. 6). Based on ANOVA with Tukey's *post-hoc* comparisons, mCherry + ve SGN population counts ($n = 3$ per time period) for the whole spiral ganglion region visualized with in situ 3D Lightsheet imaging, were not significantly different between P1 (mean = 207.7 ± 23.8) and P7 (371.7 ± 54.2; $P = 0.4029$) but increased ~ 5× from birth by P14 (1068.7 ± 22.3; $P < 0.0001$). The population declined from this peak at P30 (748.0 ± 61.4; $P = 0.0125$) and by 12 weeks (adult) was equivalent to that at birth (218.7 ± 51.0; $P > 0.9999$ compared with P1).

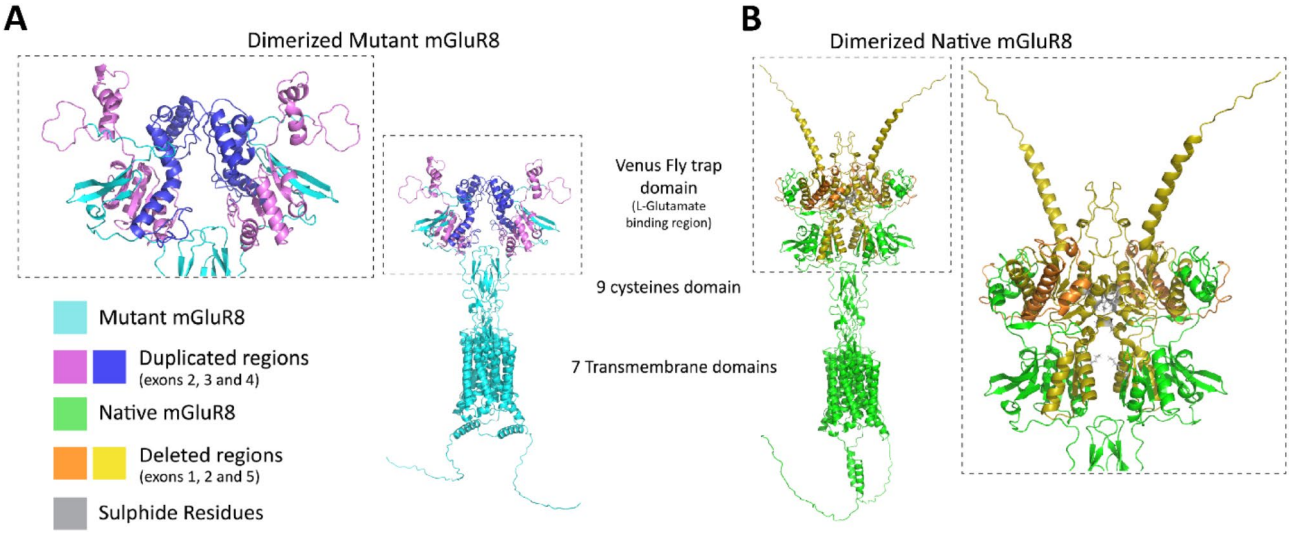

Fig. 4. AlphaFold2 modelling of mutated mGluR8 associated with *Prph*$_p$-mCherry transgene integration. AlphaFold 2.0 - based structural modelling of the effects of the exon deletions and duplications in *Grm8*, produced by the *Prph*$_p$-mCherry transgene integration in mouse Line 43. The dimerized mutant (**A**) mGluR8 protein shows pronounced structural differences at the glutamate binding site (Venus fly trap) domain. Pink highlighting delineates amino acid affected by duplicated exons; blue represents unchanged amino acid domains. The difference in steric effects has caused the disulphide bridge (9 cysteines domain) to be further apart than in the native mGluR8. The 7 transmembrane domain regions are equivalent for the native and mutated protein isoforms. The native (**B**) *Grm8* gene shows the N-terminal region sites lost by integration of the *Prph*$_p$-mCherry transgene (deleted exons; yellow and orange). Visualised with Pymol (Ver 2.5.0). Videos of the mutant Grm8 dimer and native dimer are provided as Supplementary Video 1.

An equivalent analysis was performed for the peripherin + ve SGN. As previously reported, this type II SGN population nearly halves in the first postnatal week[25]. Here, 3D spatial reconstruction enabled total type II SGN population counts: P1 mean = 1269.3 ± 220.6; P7 mean = 418.0 ± 18.3; P14 mean = 531.0 ± 4.7; P30 mean = 431.0 ± 14.7; adult mean = 430.0 ± 22.5. The type II SGN population at P1 was significantly greater than at all other time points ($P < 0.0001$ for all comparisons against P1), with population counts from P14 to adult being stable (min. $P = 0.736$).

These data clearly demonstrate the separation of the mCherry + ve and peripherin + ve neuron populations, particularly regarding the relative paucity of mCherry SGN labeling in the upper cochlea. At P1 the mCherry + ve SGN population was only ~ 15% of the size of the peripherin + ve SGN population, whereas at P14, it was ~ 200%, reducing to ~ 50% in adult. Underlying these substantial variations, the type II SGN (peripherin + ve) population that co-express mCherry remained relatively constant, although after P14 the spatial representation becomes qualitatively more focused to the hook region of the cochlea (Fig. 6): whole mCherry – type II SGN population counts: P1 mean = 47.3 ± 23.7; P7 mean = 72.7 ± 27.4; P14 mean = 237.5 ± 38.8; P30 mean = 144 ± 23.4; adult mean = 57.3 ± 26.8; (min. $P = 0.3635$, P1 vs. P14).

In the immediate postnatal period, type I SGN peripheral neurites (radial fibers) establish single punctate synapses with the IHC. Alongside this, the type II (peripherin + ve) SGN fibers initially project transiently to the IHC, as well as descending to the floor of the tunnel of Corti to establish basally tracking outer spiral fiber bundles which make *en passant* synapses with up to 30 OHC[1,2]. Both these types of SGN neurites (radial fibers and outer spiral fibers) were immunolabeled for mCherry (Fig. 7). At P1, the peripherin immunolabeling of (type II) SGN neurites was strongest, while labeling within the somata was minimal. This contrasted with the pronounced basal region mCherry somata and neurite labeling, (including the double-labeled type II SGN) which was most pronounced at P14. This double immunolabeling of the type II SGN outer spiral bundle fibers is shown alongside peripherin + ve / mCherry -ve radial fibers in the basal region at P14 (Fig. 7E); immunofluorescence signal declines in both neurite types by P30 (Fig. 7; Supplementary Video 2: Part 3).

Validation of mCherry + ve spiral and vestibular ganglion neuron sub-populations against β-III tubulin immunofluorescence

To characterize the neuronal identity of mCherry + ve neuron sub-populations not co-expressing peripherin, TUBB3 immunostaining (β3 tubulin marker) was used to generally resolve SGN and VGN. Both 3D in situ Lightsheet imaging (Figs. 8 and 9) and confocal imaging of cryosections (Figs. 10 and 11) were utilized. This confirmed that *Prph*$_p$-mCherry + ve cells were neuronal. The *in situ* imaging (n = 3–6 inner ear samples per time point) provided complementary estimates of total mCherry + ve SGN and VGN populations. SGN mCherry + ve cell counts: P1 = 199 ± 20.5; P7 = 351.8 ± 22.3; P14 = 564.5 ± 27.4; P30 = 341.8 ± 13.6; Adult = 201 ± 12.1. Note that these counts replicate the estimates provided from tissue co-immunolabeled for peripherin (Fig. 5F). VGN mCherry immunopositive cell counts across the entire VGN: P1 = 1010.3 ± 99.4, P7 = 1235.4 ± 70.6;

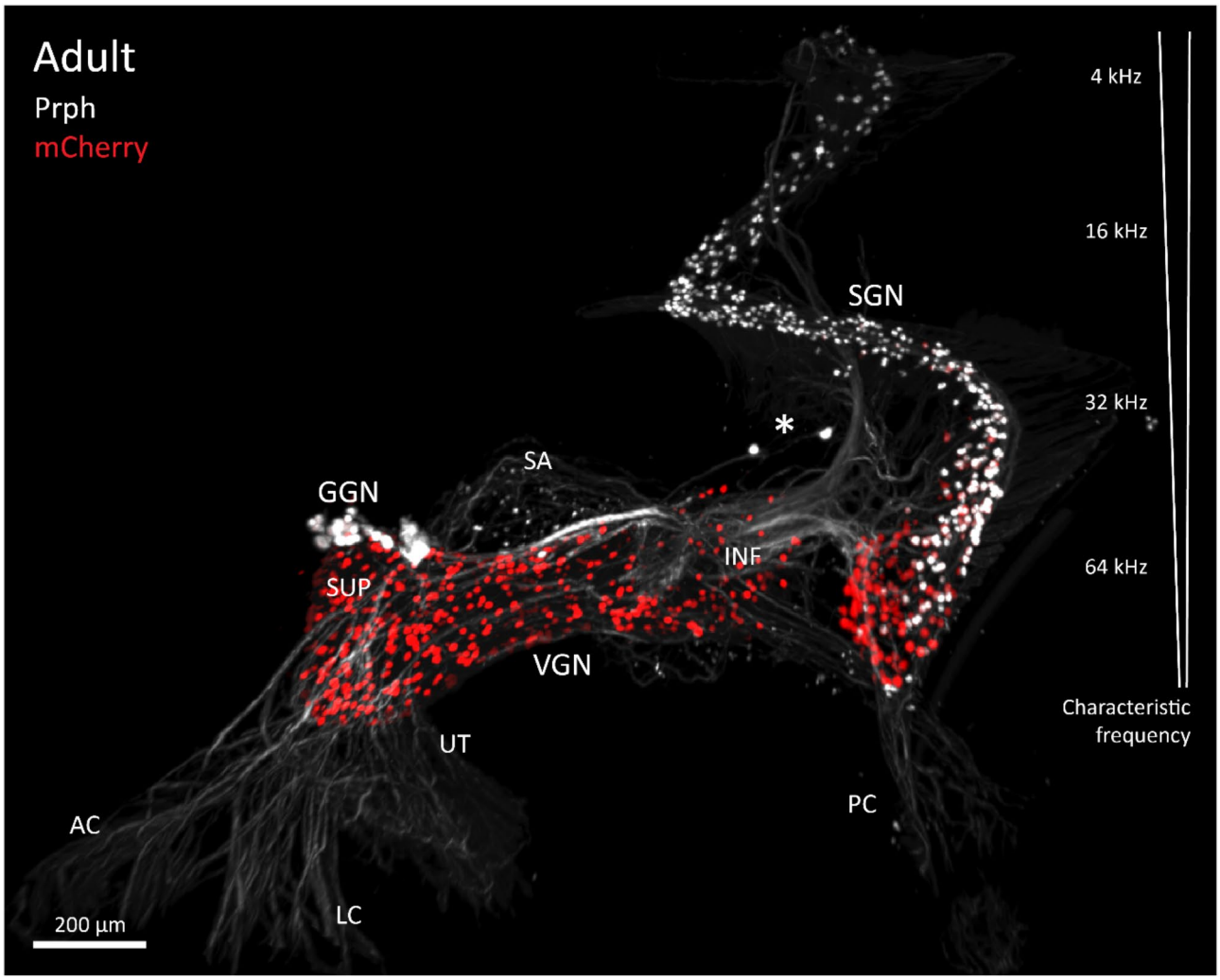

Fig. 5. mCherry reporter immunolabeling resolves subpopulations of cochlear spiral ganglion neurons (SGN) and vestibular ganglion neurons (VGN) in the intact adult mouse inner ear. Intact adult $Prph_p$-mCherry mouse inner ear tissue cleared with CUBIC/PEGASOS, imaged using Zeiss Z1 Lightsheet microscopy, rendered and analyzed with Imaris (v.9.1). Distribution of mCherry + ve (red) SGN and VGN, with co-immunolabeling against peripherin (Prph, white). Prph is a marker for cochlear type II SGN (innervating outer hair cells), and VGN whose afferents terminate as boutons on type II hair cells. mCherry + ve SGN are biased to the base, particularly the hook region (highest frequency). In contrast, mCherry + ve VGN are broadly distributed across both the superior (SUP) and inferior (INF) regions. Prph + ve peripheral VGN neurites project to all vestibular end-organs (saccule (SA), utricle (UT), semicircular canals (anterior (AC), lateral (LC), posterior (PC)). Two large Prph + ve bipolar neurons of undetermined significance were located outside of Rosenthal's canal in the cochlear modiolus (*). Geniculate ganglion neurons (GGN; facial nerve VII) reside above the VGN; most of the GGN in this sample were outside the volume rendering. This image has removed non-specific puncta with segmentation, to aid in visualization of elements of interest. A characteristic frequency map of the tonotopically-organized cochlea is shown.

P14 = 1010.5 ± 50.5; P30 = 653.2 ± 8.1; Adult = 589.8 ± 46.4. The mCherry + ve VGN were evidently biased towards the superior nucleus relative to inferior nucleus, particularly at P1 when the latter was less differentiated (Fig. 8A′), and this difference was consolidated through to the adult (Figs. 5 and 8E′). Defining the VGN subnuclei boundaries was problematic and quantitation of densities within these subnuclei was not pursued.

An estimate of the proportion of mCherry + ve somata within the total neuronal populations was undertaken using double immunolabeling of cryosections against mCherry and TUBB3. The predominance of $Prph_p$-mCherry SGN within the hook region was maintained throughout development (Fig. 10) compared to basal (min $P = < 0.0001$) and apical regions (min $P = < 0.0001$) although the proportion of hook region mCherry + ve neurons was the least at P30 and adult (ANOVA Bonferroni multiple comparison tests; $n = 5–11$ regional counts per age; P values reflective of all ages). The double immunolabeled cryosections showed that 92% of P1 hook region SGN were mCherry + ve. The proportion of TUBB3 + ve – mCherry -ve neurons in this region increased over time, reducing the proportion of mCherry + ve neurons progressively: mean proportions P1 = 0.918 ± 0.030;

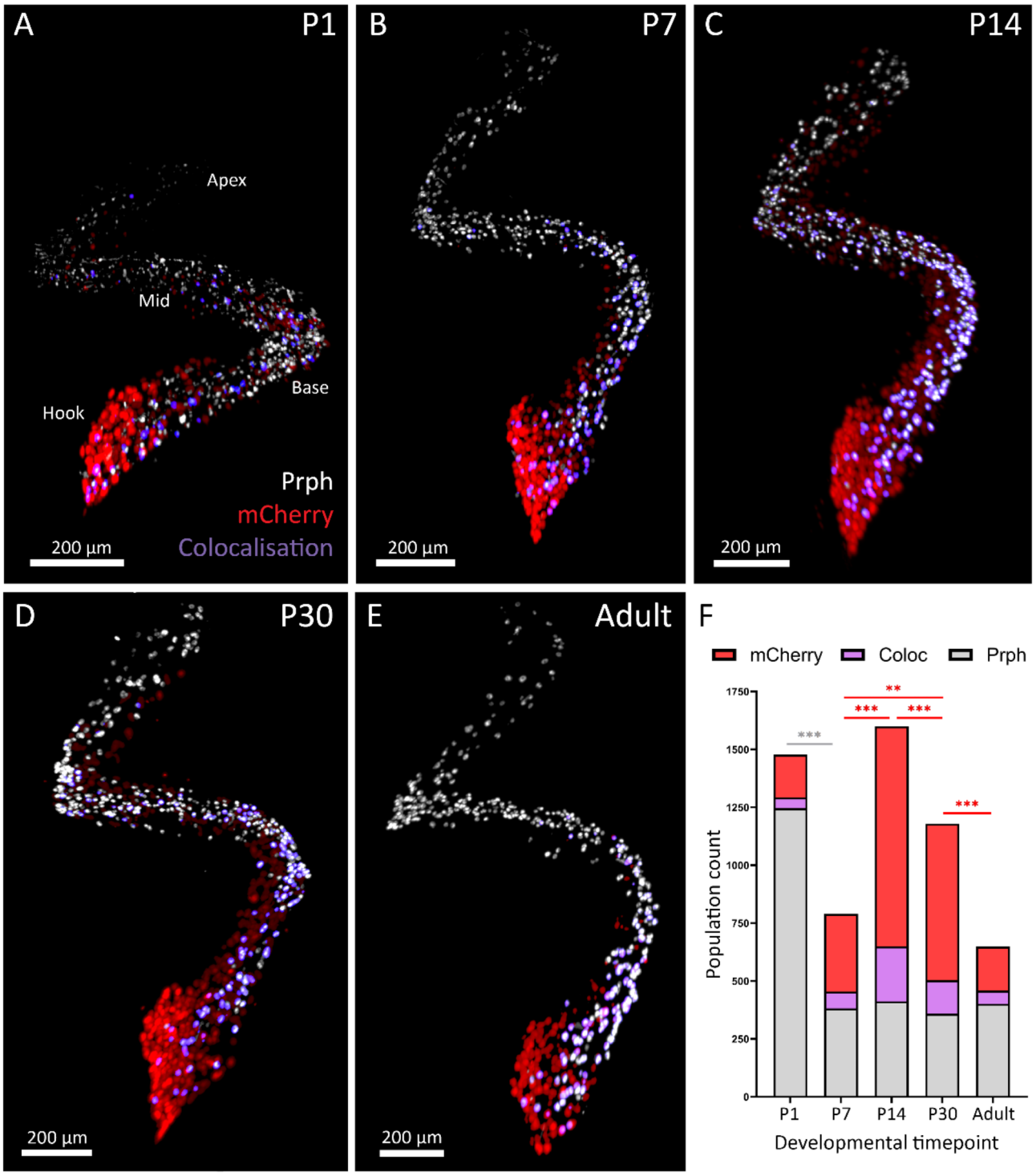

Fig. 6. Postnatal variation in mCherry - reporter and peripherin + ve SGN populations, including co-immunolocalization. (**A**–**E**) mCherry (red) and peripherin (white) immunolabeling of SGN across postnatal days 1, 7, 14, 30 and adult intact cochleae. Type II SGN (peripherin + ve) co-labeled for mCherry are shown in purple. (**F**) Graphical analysis of proportional SGN population counts. Counted as 'spots' in Imaris; n = 3 for all developmental timepoints (individual cell count data provided as Supplementary Table 3). PEGASOS / Lightsheet / Imaris SGN segmentation and masking.

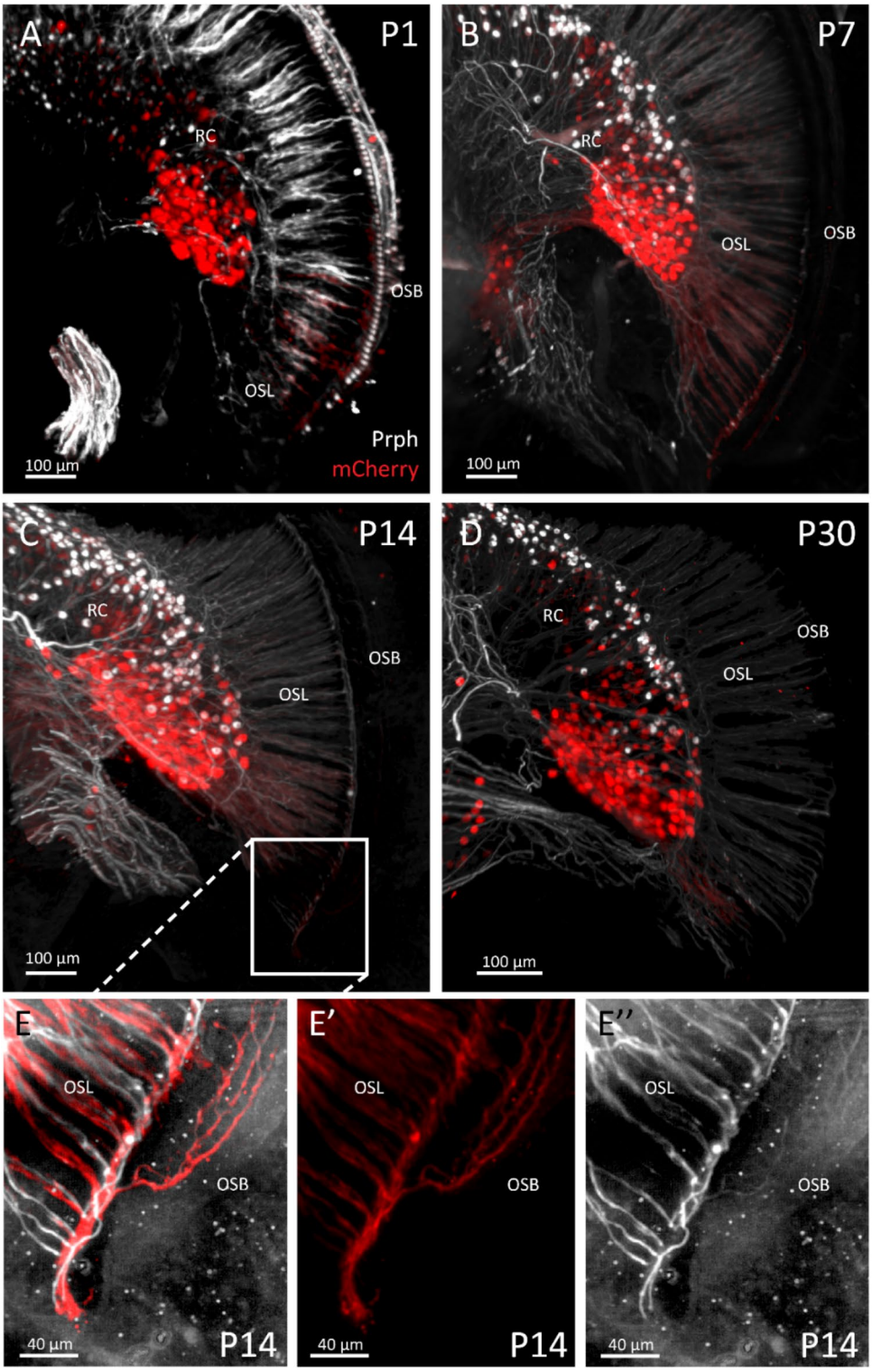

Fig. 7. Development of SGN neurites in the basal cochlea of the *Prph*$_p$-mCherry mouse. (**A**–**D**) Peripherin (white) and mCherry (red) immunofluorescent staining in postnatal day 1, 7, 14 and 30 cochleae intact samples. These samples are oriented to focus on the hook region of the spiral ganglion. SGN cell bodies reside in Rosenthal's canal (RC), their fibers project to the two hair cell populations via the osseous spiral lamina (OSL). Fibers travelling below the hook region are projecting from the vestibular ganglion to the posterior RC. (**E**, **E**′, **E**″) Illustrate the combination of radial fiber co-labeling (IHC target) and the outer spiral fibre co-labeling (OHC target). PEGASOS / Lightsheet / Imaris processing with non-specific immunolabeling manually reduced in the background of these images.

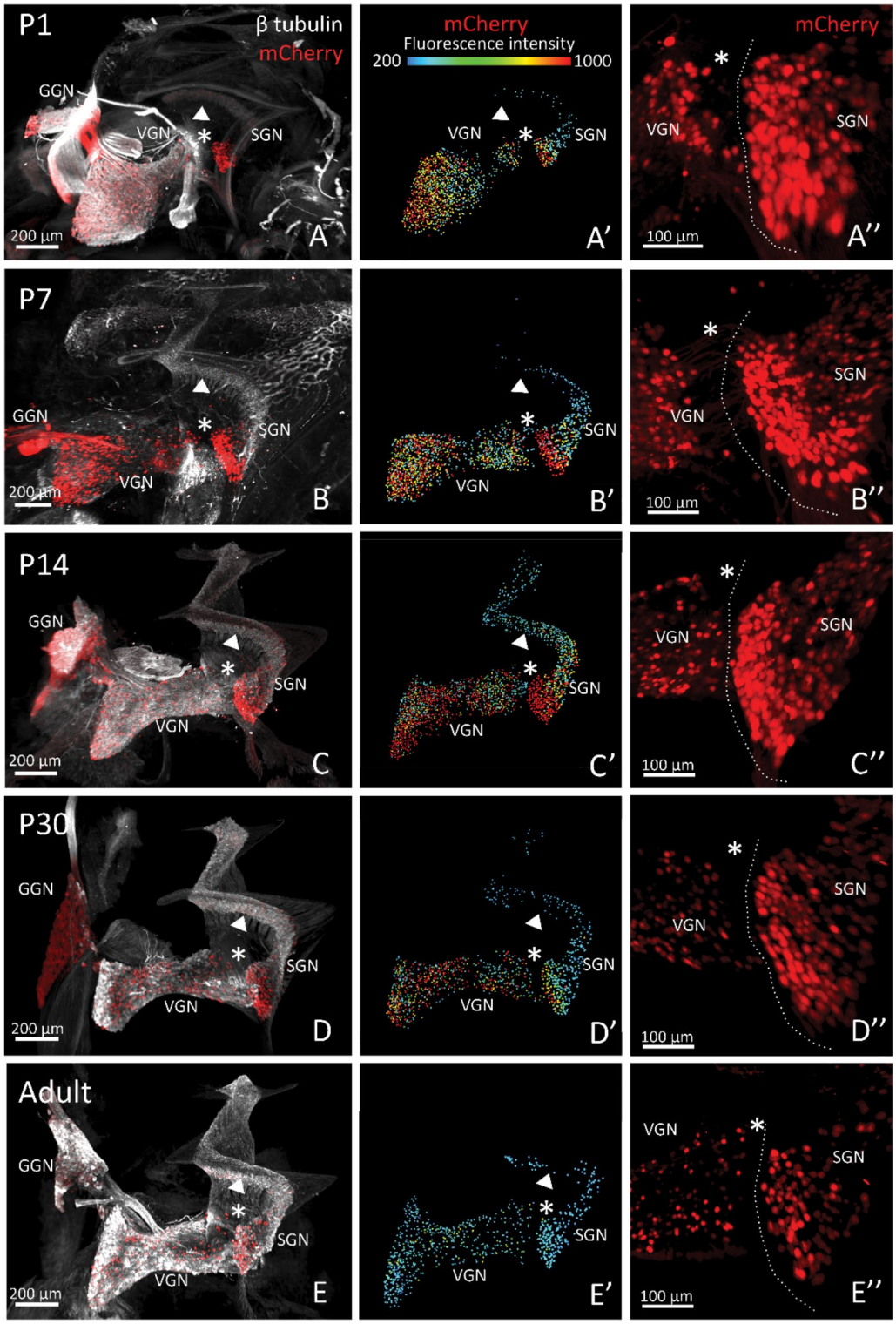

Fig. 8. Localization of mCherry and β3-tubulin (TUBB3) immunolabeling of cochlear spiral ganglion (SGN) and vestibular ganglion (VGN) somata through postnatal development. (**A**–**E**) Postnatal (P) whole inner ear in situ Lightsheet imaging segmented to resolve the somata using Imaris software: P1, P7, P14, P30 and Adult (10–16 weeks). Arrows show Rosenthal's canal where the somata of the SGN population are located. * indicates ROI at the confluence of the SGN hook region and VGN inferior region, shown in **A**″–**E**″. (**A**′–**E**′) Pseudo-colour intensity-mapping of segmented mCherry + ve neurons throughout the SGN and VGN. (**A**″–**E**″), Dashed line indicates the separation of the spiral and vestibular ganglia. GGN, geniculate ganglion of the facial nerve (VII) also exhibits pronounced mCherry immunolabeling.

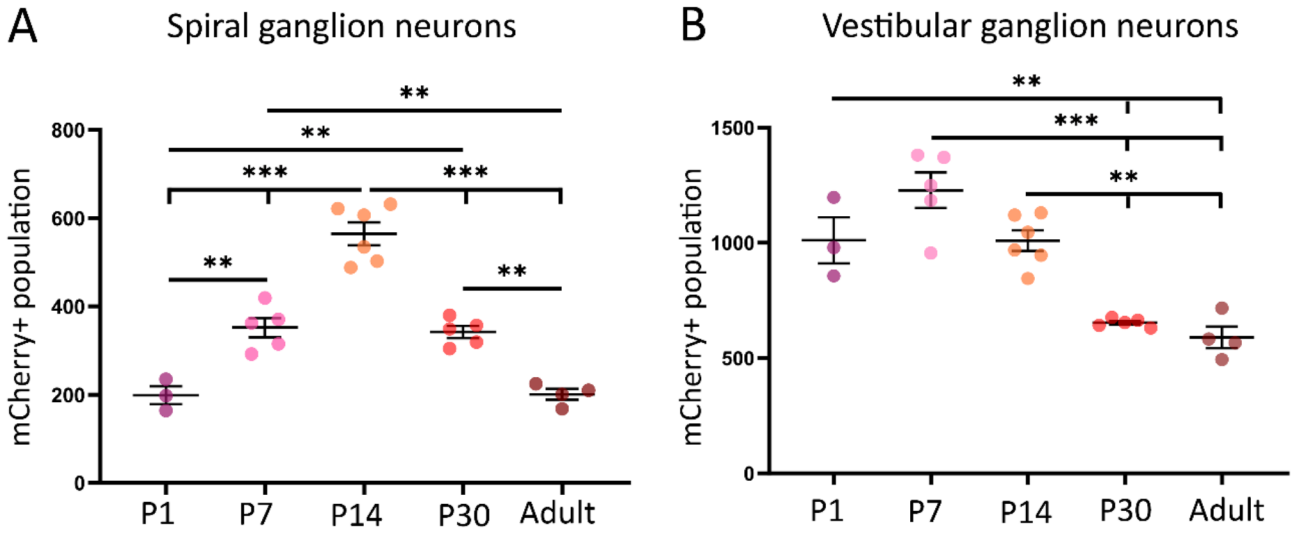

Fig. 9. Graphical analysis of *in situ* mCherry + ve spiral ganglion neurons (SGN) and vestibular ganglion neurons (VGN) cell counts across all regions during postnatal development. (**A**) Whole population counts for the mCherry + ve SGN. (**B**) Whole population counts for the VGN. ** $P \leq 0.007$; *** $P \leq 0.0001$; ANOVA with Tukey's multiple comparisons *post-hoc* tests. Block processed inner ear tissue with PEGASOS for mCherry and TUBB3 immunolabeling and imaged using Lightsheet; postnatal day 1 (P1) to adult. Mean and s.e.m., with individual data overlay.

P7 = 0.745 ± 0.080; P14 = 0.656 ± 0.057; P30 = 0.551 ± 0.059; Adult = 0.418 ± 0.054 ($P = 0.2635$; 0.002, < 0.0001, < 0.0001 comparing P7 – adult against P1, respectively; ANOVA Bonferroni *post-hoc* comparisons). The relative size of the mCherry + ve neurons within the SGN across postnatal development was quantified in the cryosection samples. P7 (mean = 125.58 ± 21.51 μm^2) and P14 (mean = 122.24 ± 21.07 μm^2) exhibited populations with an increase in cross-sectional areas over other ages (Fig. 10G).

In the VGN, the proportion of mCherry + ve neuron relative to TUBB3 + ve / mCherry -ve neurons reduced over time (Fig. 11A-F). Proportion means: P1 = 0.796 ± 0.112; P7 = 0.580 ± 0.062; P14 = 0.221 ± 0.074; P30 = 0.115 ± 0.015; adult = 0.141 ± 0.004. The proportion of the VGN mCherry + ve population stabilized after P14. ANOVA with Bonferroni *post-hoc* comparisons indicated significant differences for P1 and P7, P7 vs. P14 - adult ($P < 0.01$). mCherry + ve VGN cell size reduced after postnatal development (ANOVA $P < 0.001$; $n = 3$ per time), with adult VGN showing smaller cell sizes compared to all other timepoints (min $P = 0.02$). Mean mCherry + ve VGN surface areas: P1 = 121.15 ± 25.84 μm^2; P7 = 158.06 ± 32.90 μm^2; P14 = 129.54 ± 21.41 μm^2; P30 = 112.79 ± 23.15 μm^2; adult = 80.19 ± 11.80 μm^2 (Fig. 11G).

Multi-channel confocal immunofluorescence imaging of the vestibular end-organs demonstrated the overlap of a subset of Prph + ve bouton afferents with the mCherry reporter. In the semicircular canals, the mCherry + ve afferent terminals were predominantly bouton afferents projecting to the type II hair cell in the isthmus region of the crista ampullaris, with a small subset of mCherry + ve Calyx afferents indicating innervation of type I hair cells (Fig. 12). Immunolabeling of the peripherin and mCherry + ve vestibular neurites was absent in the adult vestibular end-organs (and the organ of Corti), suggesting down-regulation of expression.

Evaluation of hearing function of Prph$_p$-mCherry transgenic mouse

Auditory brainstem response (ABR) threshold analysis in adult mice (13–15 weeks of age) suggested that the *Prph*$_p$-mCherry transgenic reporter mice had reduced hearing sensitivity towards the basal (higher frequency encoding) region. This may reflect a functional impact on the type I mCherry + ve SGN afferents. While click ABR thresholds (reflecting lower frequencies) were similar (*Prph*$_p$-mCherry = 35.8 ± 2.8 dB SPL, $n = 6$; WT = 35.4 ± 2.8 dB SPL, $n = 6$; $P = 0.939$, multiple comparison Bonferroni t-test), average ABR thresholds for tone pips were typically higher for the *Prph*$_p$-mCherry genotype (4–24 kHz); with a maximum difference at 24 kHz ($P = 0.004$; multiple comparison Bonferroni t-test)) (Fig. 13A,B). There was no significant difference in the supra-threshold growth functions (55–70 dB SPL) between genotypes (*Prph*$_p$-mCherry gain: 61.2 ± 5.7 nV/dB for N1-P2 wave at 24 kHz; WT: 37.7 ± 7.2 nV/dB; $n = 4$ per genotype; $P = 0.0571$; Mann Whitney ranked test) (Supplementary Fig. 4). In comparison, analysis of the cubic DPOAE ($2f_1$-f_2) thresholds, which report sound transduction at the cochlear OHC, showed no genotype effect (8–24 kHz; $P = 0.981$, repeated measures Two-way ANOVA) (Fig. 13C,D). We found a proportionate drive increase, but generally a higher recruitment with delayed thresholds is observed in the *Prph*$_p$-mCherry mice.

Discussion

In situ 3D Lightsheet imaging of *Prph*$_p$-mCherry transgenic mouse Line 43 resolved discrete subpopulations of cochlear and vestibular neurons. In the cochlea, the majority of basal-most ('hook') region SGN were mCherry + ve. This corresponds to both the highest frequency encoding type I SGN innervating IHC (~ 60–90 kHz)[53] and the

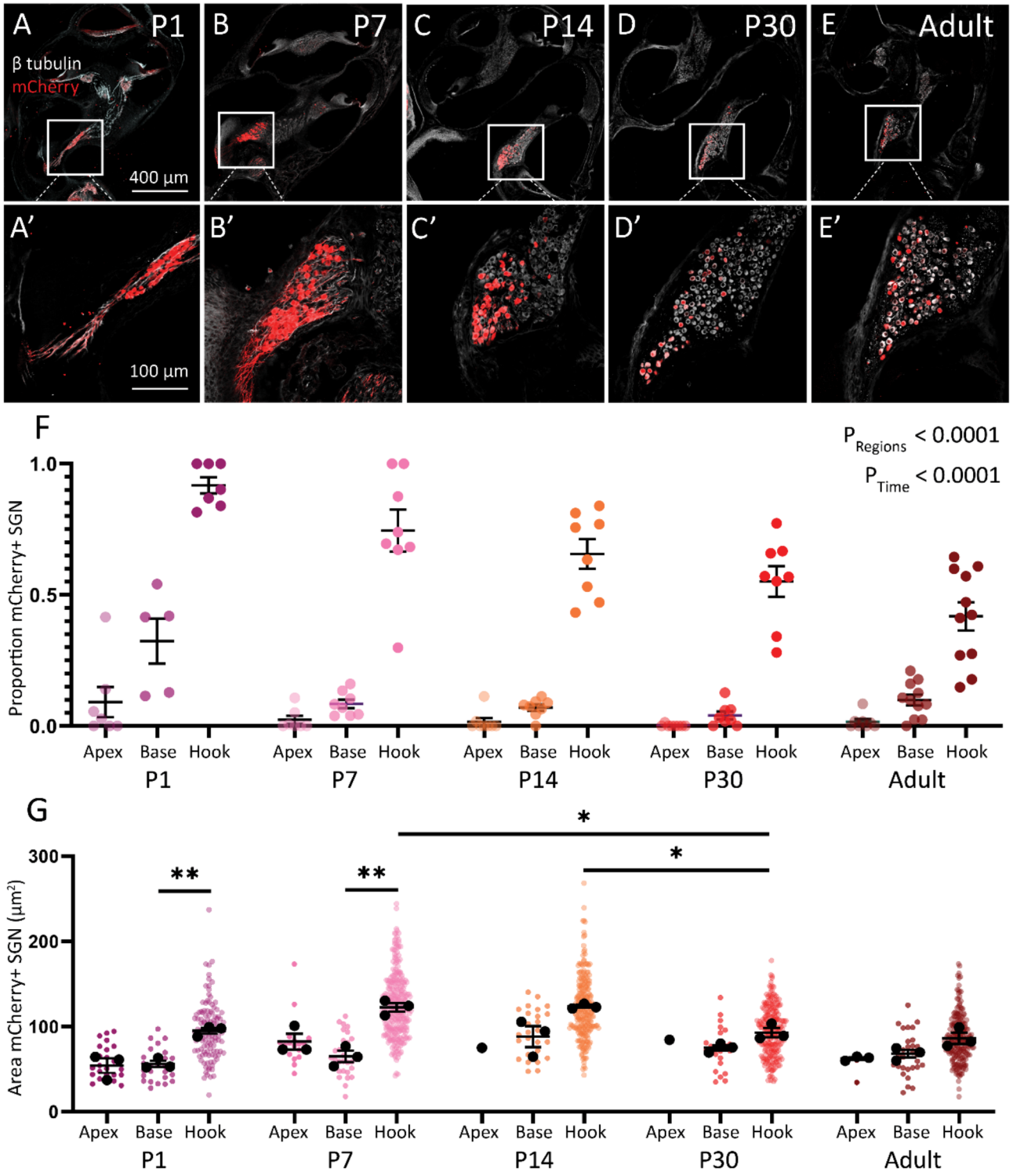

Fig. 10. Variation in proportion and size of mCherry +ve SGN through postnatal development. (**A**–**E**) Overview of sections throughout development. (**A**′–**E**′), Reduction in hook region expression of mCherry + ve SGN in sections double immunolabeled for mCherry and TUBB3. **F**, Graphical analysis of changes in mCherry proportion relative to TUBB3 (mCherry negative) neurons across regions through postnatal development (P). Colored dots show the population count for each mouse. Statistical comparisons were performed with two-way ANOVA and Holm-Sidak *post-hoc* comparisons test. Refer to Supplementary Table 4 for statistical comparisons. (**G**) Cross-sectional relative areas of mCherry + ve neurons in different regions of the spiral ganglion. mCherry immunolabeled SGN data combined from 3 cryosections per region / time point (black spots represent individual means). Mean and s.e.m., with individual data overlay of biological repeats. Colored dot overlay reports individual cells across all samples. Black bars indicate the comparisons with significant differences.

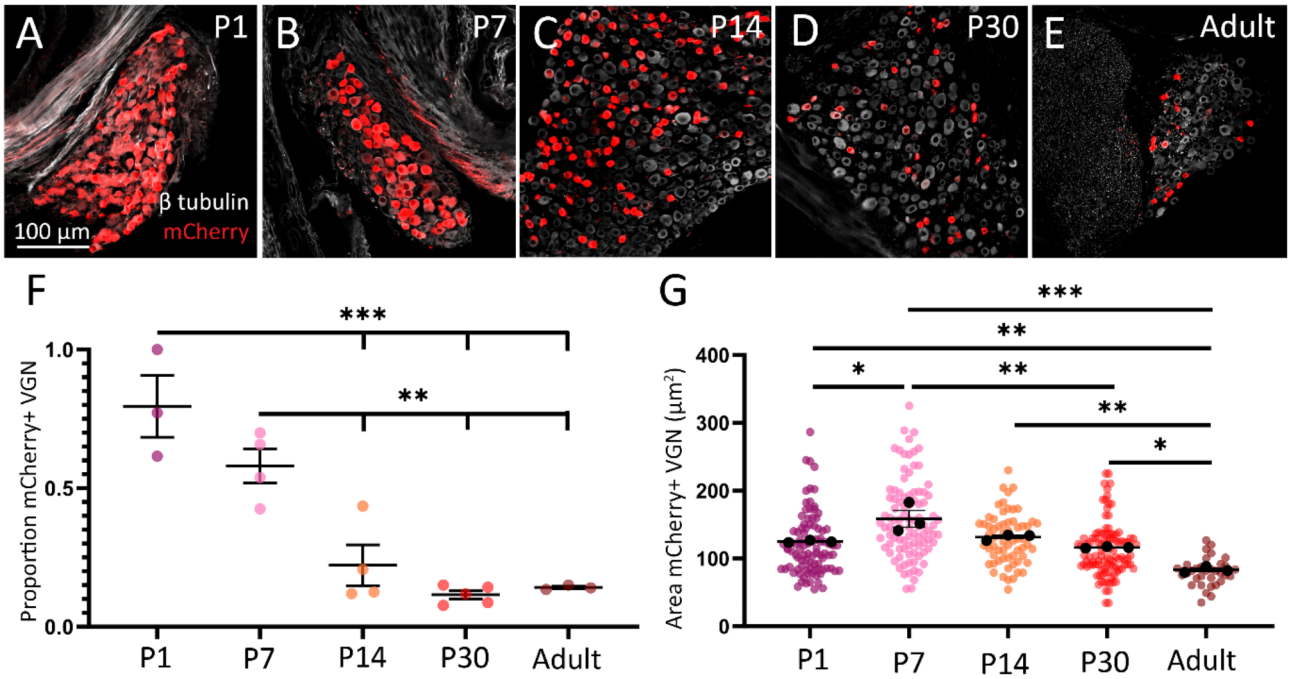

Fig. 11. mCherry + ve vestibular ganglion neuron proportion and size through development in the inner ear. (**A**–**E**) Visualization of neurons through TUBB3 (white) and the *Prph*$_p$-mCherry population (red) at postnatal (P) days 1, 7, 14, 30 and adult. (**F**) Decline in proportion of mCherry + ve VGN compared to TUBB3 + ve VGN across developmental timepoints. Mean and s.e.m. individual data overlay reflect data from cryosections from different mice. (**G**) Relative size of mCherry + ve VGN across development timepoints. ** $P \leq 0.007$, *** $P < 0.001$, ANOVA Bonferroni multiple pairwise comparison. Mean and s.e.m., with individual data overlay of biological repeats (combining sampling from 3 cryosections / mice per time point). Colored dot overlay reports individual cells across all samples. Black bars indicate the comparisons with significant differences.

(Prph + ve) type II SGN innervating the OHC. The density of mCherry + ve SGN declined towards the apex, and expression intensity diminished after P14. In contrast to regional delineation of subpopulations of cochlear type I and type II SGN, mCherry reporter expression in the vestibular ganglion was distributed within the superior and inferior regions, as small-diameter VGN, known to correspond to bouton afferents[22] innervating the otolith organs and semicircular canals.

The *in situ* visualization of SGN Prph immunofluorescence enabled the first total type II SGN neuron population counts (shown to diminish from 1270 at P1 to 430 in adult), associated with consolidation of the outer spiral fiber innervation of OHC[25]. With postnatal development, the mCherry + ve SGN population increased in the early postnatal period, despite this loss of type II SGN, reflecting the dominance of the mCherry + ve type I SGN subpopulation.

Prph$_p$-mCherry transgene integration occurred in the N-terminal coding region within the extended (850 kb) *Grm8* gene. Given that three other *Prph*$_p$-mCherry transgenic mouse lines failed to resolve SGN and VGN subpopulations, while exhibiting strong dorsal root ganglia (DRG) expression (as predicted by previous transgenic mouse models using the *Prph*$_p$[29]), this suggests that in this Line 43, the integration of the transgene within the *Grm8* reading frame contributed to regulatory control of mCherry reporter expression. The potential influence of *Grm8* integration on neuronal subtype selectivity of *Prph*$_p$-mCherry transcription may be associated with an open chromatin environment[54] facilitating transcription factor and RNA polymerase access. While *Grm8* is expressed by multiple sensory and supporting cell types throughout the cochlea[55], it is selectively expressed by type Ic SGN[13,56], based on scRNAseq mRNA transcript clustering. Here, in *Prph*$_p$-mCherry mouse Line 43, disruption of the *Grm8* gene, including the loss of the glutamate binding domain (associated with exons 1–5[57]), likely places the homozygous *Prph*$_p$-mCherry transgene on a functional null *Grm8* background, despite the potential for anomalous mRNA transcription. A prior transgenic *Grm8* knockdown mouse model lacked a hearing loss phenotype[58], in the current study ABR hearing testing of the *Prph*$_p$-mCherry Line 43 mouse showed a very mild loss of hearing sensitivity, which support the prior data indicating that *Grm8* is dispensable for hearing. The observed elevation in thresholds in Line 43 *Prph*$_p$-mCherry mice may indicate a change in functionality of the type Ic SGN[59] particularly in the higher frequency region. It is notable that scRNAseq studies have established that type Ic SGN are in a higher proportion at the base of the cochlea[15,60].This is supported by equivalency of sound transduction by the (outer) hair cells evident from the similarity in DPOAE thresholds between genotypes. Given the hearing phenotype of the Line 43 *Prph*$_p$-mCherry mice revealed by ABR, future studies could evaluate potential impacts on vestibular function.

The *Prph*$_p$-mCherry mouse line was designed to report the native peripherin type III intermediate filament expression, as a marker of the type II SGN[1,24–26]. Notably, this expected distribution was confined to the basal-

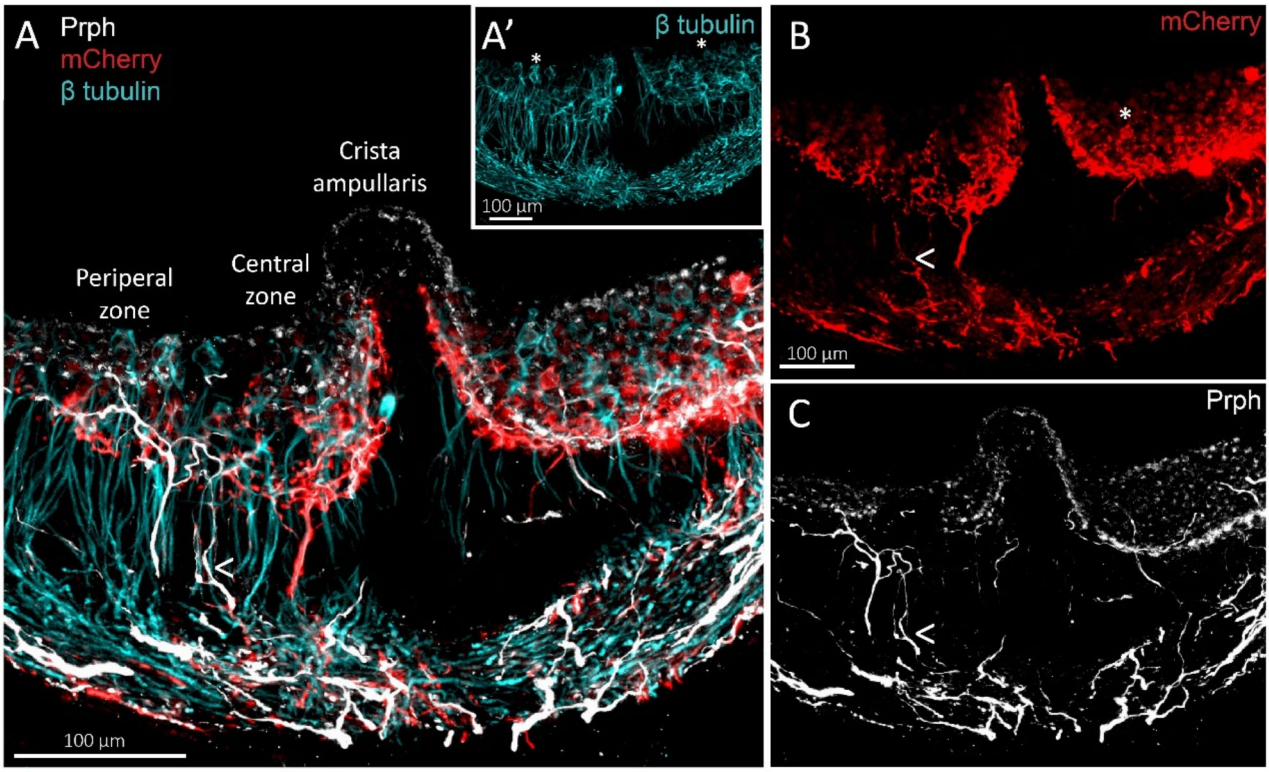

Fig. 12. Vestibular afferent innervation of the posterior semicircular canal labeled by mCherry, peripherin (Prph) and TUBB3 (β3-Tubulin) immunofluorescence. (**A**) Combined confocal immunofluorescence; 50 µm cryosection P30 *Prph*$_p$-mCherry mouse tissue; inset (**A**′) shows TUBB3 immunofluorescence labeling of the VGN afferent terminal population in the end-organ; * indicates representative calyx synapse on the type I hair cells, while the bouton afferents extend uniformly across the breadth of the sensori-epithelium to synapse with type II hair cells. (**B**) mCherry channel indicating a predominance of bouton-type VGN afferent fibers terminating in the isthmus region of the crista ampullaris; * indicates mCherry + ve calyx afferent synapse; arrowhead indicates bouton afferent doubled immunolabeled for Prph (see also **A** and **C**). (**C**) Prph immunolabeling of a subset of bouton afferents with distributed puncta within the sensori-epithelium.

most aspect of the cochlea where all (Prph-immunopositive) type II SGNs colocalized with mCherry, albeit alongside mCherry expressing type I SGN. The incorporation of the P1 and P2 peripherin promotor and repressor elements into the *Prph*$_p$ construct were developed to achieve an improved authenticity of transgene expression across the breath of sensorimotor cranial and peripheral nerves[27,29,31], but this has not previously been established for spiral and vestibular ganglia. The influence of the broader gene regulatory environment on Prph expression is also evident from mouse[61] and human[62] bacterial artificial chromosomes (BACs) GFP transgene knockin models, where ~150 kb of flanking genomic DNA is integrated. Peripherin expression of human BAC *Prph - GFP* reporter knockin was examined in the mouse cochlea (Elliott et al., 2021b), where there was a strong match to the profile of native Prph expression detected using immunohistochemistry[9].

The drop-off in Prph levels in the peripheral neurites beyond postnatal week 1 reported in both these studies was matched here to the change in type II SGN Prph and mCherry co-immunolocalization. While Prph immunolabeling in the outer spiral bundle was greatly reduced by P14 beyond the osseous spiral lamina (Fig. 7E"), the mCherry immunolocalization to distal neurites (cochlear hook region and vestibular end-organs (Fig. 12), was sustained to P30, but strongly down-regulated in the adult, alongside a precipitous reduction of 70% in detectable mCherry +ve SGN beyond P30. These findings suggest that cochlear ontogeny dynamics proceeds well into the perceived 'mature' phase.

Studies of embryonic inner ear development indicate that the basal turn SGN exit the cell cycle in the otic placode before apical neurons[63–65]. Similarly cochlear afferent ontogeny in the early postnatal period is driven from the base, with consolidation of the innervation of the sensory hair cells delayed by several days in the apex[64]. In parallel with this, there is differentiation of the type I and type II SGN, defined by synaptic pruning which consolidates the former to single puncta synapses at single IHC, while the type II SGN either establish extended multi-OHC *en passant* synapses, or are lost through apoptosis prior to hearing onset in postnatal week 2 of mouse[25] and rat[66] development. This ontogenic programming contrasts with the delineation of the cochlear SGN subpopulations by the mCherry reporter, where the expression profile builds soon after hearing onset (Figs. 7 and 9). In the vestibular system Prph is known to be a key neurofilament for supporting neural outgrowth and survival in unmyelinated and small diameter sensory neurons[30]. The *Prph*$_p$-mCherry Line 43

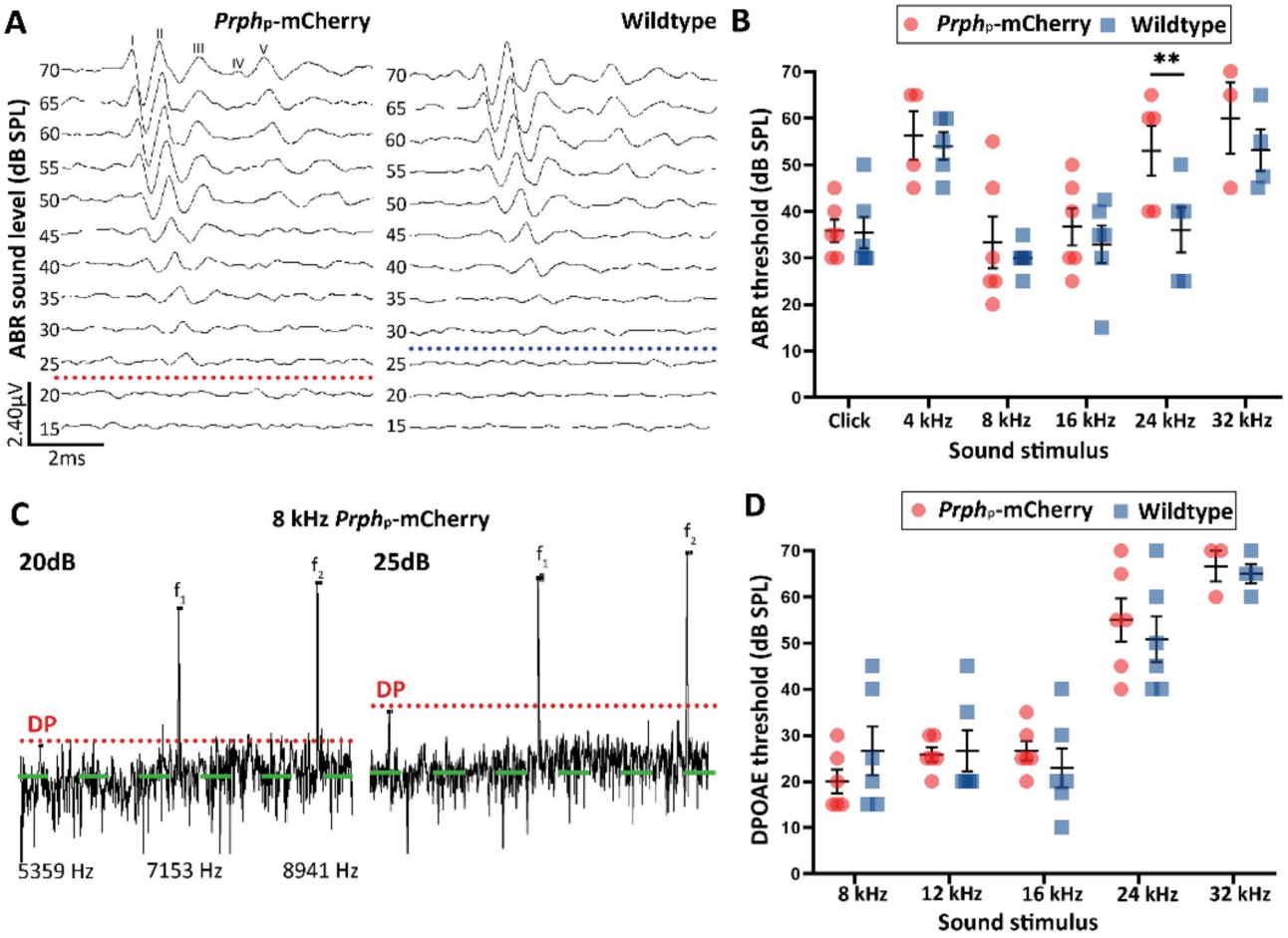

Fig. 13. Hearing performance of *Prph*$_p$-mCherry transgenic mice against age-matched wildtypes (WT). (**A**) Example of auditory brainstem response (ABR) traces (10 ms) using an 8 kHz tone pip for decreasing intensity to establish threshold. Data from a WTe (30 dB SPL threshold) and a *Prph*$_p$-mCherry mouse (25 dB SPL threshold). The peaks of the ABR waveform have been labeled where Peak I represents the auditory nerve activity prior to the cochlear nucleus, waves II – IV arise from synchronous firing at auditory sites in the hindbrain, and wave V stems from the inferior colliculus level. (**B**) ABR threshold population data; * $P < 0.05$, t-test. (**C**) Example of fast Fourier transformed 8 kHz DPOAE data from a *Prph*$_p$-mCherry mouse; f_1 (7153 Hz) and f_2 (8941 Hz) drivers at 20 dB SPL (threshold) and 25 dB SPL (supra-threshold); ($2f_1 - f_2$) distortion product (DP) (5359 Hz) (dashed red lines). The green dashed line indicates the noise floor. (**D**) DPOAE population data. *Prph*$_p$-mCherry $n = 7$; WT $n = 6$. * indicates t-test $P < 0.05$. ANOVA across frequency levels for both ABR and DPOAE data indicated no significant differences between genotypes ($P > 0.05$). Bar graphs show mean ± s.e.m., with individual data overlay.

vestibular system demonstrates progressive refinement of mCherry expression to smaller sized VGN. The literature is sparse with regard to postnatal vestibular neural development, but the data from the present study suggests that the small diameter VGN bouton afferents innervating the type II vestibular hair cells may undergo programmed cell death as found for the type II SGNs, but mapped to the prolonged differentiation of the otolith maculae[18,22,67].

Recent advances in genetic technologies, transgenic models, scRNAseq, in situ hybridization and fluorescence microscopy are extending our understanding of the development of inner ear primary afferent diversity beyond the classical structure/function delineations[15,56]. The *Prph*$_p$-mCherry reporter model, with 3D in situ characterization, provides a new resource for this challenge, by identifying subpopulations of cochlear type I and type II SGN, particularly distinguishing a cluster of ~ 500 SGN in the extreme base (hook), including the anticipated ~ 5% of type II SGN; while *Prph*$_p$-mCherry reporting in the VGN consolidated to small diameter afferents. This model provides an opportunity to extend the characterization of these inner ear afferents using spatial proteomics and transcriptomics tied to mapping of the mCherry reporter subpopulations. Inclusion of a human diphtheria toxin receptor element within the *Prph*$_p$-mCherry transgene enables future studies evaluating impact of selective neuronal ablation on hearing and balance, potentially both within the inner ear and where systemic application of diphtheria toxin could evaluate the loss of mCherry + ve subpopulations in the peripheral and central nervous systems. The breadth of transgene expression beyond the inner ear (not shown), enables evaluation of models of sensorimotor neural circuit development and pathophysiology pertinent to a range

of neurological disorders, particularly those associated with intermediate filament-dependent neural circuit refinement and maintenance.

Data availability

Raw DNA and annotated data can be found at ENA under project PRJEB79255.

Received: 1 November 2024; Accepted: 11 March 2025
Published online: 25 March 2025

References

1. Huang, L. C. et al. Synaptic profiles during neurite extension, refinement and retraction in the developing cochlea. *Neural Dev.* **7**, 38. https://doi.org/10.1186/1749-8104-7-38 (2012).
2. Jagger, D. J. & Housley, G. D. Membrane properties of type II spiral ganglion neurones identified in a neonatal rat cochlear slice. *J. Physiol.* **552**, 525–533. https://doi.org/10.1111/j.1469-7793.2003.00525.x (2003).
3. Vyas, P., Wu, J. S., Jimenez, A., Glowatzki, E. & Fuchs, P. A. Characterization of transgenic mouse lines for labeling type I and type II afferent neurons in the cochlea. *Sci. Rep.* **9**, 5549. https://doi.org/10.1038/s41598-019-41770-5 (2019).
4. Housley, G. D. et al. Cochlear homeostasis: a molecular physiological perspective on maintenance of sound transduction and auditory neurotransmission with noise and ageing. *Curr. Opin. Physiol.* **18**, 106–115. https://doi.org/10.1016/j.cophys.2020.09.012 (2020).
5. Flores, E. N. et al. A Non-canonical pathway from cochlea to brain signals tissue-damaging noise. *Curr. Biol.* **25**, 606–612. https://doi.org/10.1016/j.cub.2015.01.009 (2015).
6. Liu, C., Glowatzki, E. & Fuchs, P. A. Unmyelinated type II afferent neurons report cochlear damage. *Proc. Natl. Acad. Sci.* **112**, 14723–14727 https://doi.org/10.1073/pnas.1515228112 (2015).
7. Li, J. et al. Contralateral suppression of DPOAEs in mice after Ouabain treatment. *Neural Plast.* **2018**, 6890613. https://doi.org/10.1155/2018/6890613 (2018).
8. Froud, K. E. et al. Type II spiral ganglion afferent neurons drive medial olivocochlear reflex suppression of the cochlear amplifier. *Nat. Commun.* **6**, 7115. https://doi.org/10.1038/ncomms8115 (2015).
9. Cederholm, J. M. E. et al. Noise-induced hearing loss vulnerability in type III intermediate filament peripherin gene knockout mice. *Front. Neurol.* **13**, 962227. https://doi.org/10.3389/fneur.2022.962227 (2022).
10. Taberner, A. M. & Liberman, M. C. Response properties of single auditory nerve fibers in the mouse. *J. Neurophysiol.* **93**, 557–569. https://doi.org/10.1152/jn.00574.2004 (2005).
11. Petitpré, C. et al. Neuronal heterogeneity and stereotyped connectivity in the auditory afferent system. *Nat. Commun.* **9**, 3691. https://doi.org/10.1038/s41467-018-06033-3 (2018).
12. Shrestha, B. R., Wu, L. & Goodrich, L. V. Runx1 controls auditory sensory neuron diversity in mice. *Dev. Cell.* **58**, 306–319. .e305 (2023).
13. Sun, S. et al. Hair cell mechanotransduction regulates spontaneous activity and spiral ganglion subtype specification in the auditory system. *Cell* **174**, 1247–1263e1215. https://doi.org/10.1016/j.cell.2018.07.008 (2018).
14. Siebald, C. et al. Molecular signatures define subtypes of auditory afferents with distinct peripheral projection patterns and physiological properties. *Proc. Natl. Acad. Sci. U S A.* **120**, e2217033120. https://doi.org/10.1073/pnas.2217033120 (2023).
15. Shrestha, B. R. et al. Sensory neuron diversity in the inner ear is shaped by activity. *Cell* **174**, 1229–1246e1217. https://doi.org/10.1016/j.cell.2018.07.007 (2018).
16. Sadeghi, S. G., Chacron, M. J., Taylor, M. C. & Cullen, K. E. Neural variability, detection thresholds, and information transmission in the vestibular system. *J. Neurosci.* **27**, 771–781. https://doi.org/10.1523/jneurosci.4690-06.2007 (2007).
17. Goldberg, J. M. Afferent diversity and the organization of central vestibular pathways. *Exp. Brain Res.* **130**, 277–297. https://doi.org/10.1007/s002210050033 (2000).
18. Demêmes, D. et al. Identification of neuron subpopulations in the rat vestibular ganglion by calbindin-D 28K, calretinin and neurofilament proteins immunoreactivity. *Brain Res.* **582**, 168–172. https://doi.org/10.1016/0006-8993(92)90334-6 (1992).
19. Leonard, R. B. & Kevetter, G. A. Molecular probes of the vestibular nerve. I. Peripheral termination patterns of calretinin, Calbindin and peripherin containing fibers. *Brain Res.* **928**, 8–17. https://doi.org/10.1016/s0006-8993(01)03268-1 (2002).
20. Kalluri, R. Similarities in the biophysical properties of spiral-ganglion and vestibular-ganglion neurons in neonatal rats. *Front. NeuroSci.* **15** https://doi.org/10.3389/fnins.2021.710275 (2021).
21. Balmer, T. S. & Trussell, L. O. Selective targeting of unipolar brush cell subtypes by cerebellar mossy fibers. *Elife* **8** https://doi.org/10.7554/eLife.44964 (2019).
22. Lysakowski, A., Alonto, A. & Jacobson, L. Peripherin immunoreactivity labels small diameter vestibular 'bouton' afferents in rodents. *Hear. Res.* **133**, 149–154. https://doi.org/10.1016/s0378-5955(99)00065-9 (1999).
23. Elliott, K. L. et al. Developmental changes in Peripherin-eGFP expression in spiral ganglion neurons. *Front. Cell. Neurosci.* **15** https://doi.org/10.3389/fncel.2021.678113 (2021).
24. Barclay, M., Julien, J. P., Ryan, A. F. & Housley, G. D. Type III intermediate filament peripherin inhibits neuritogenesis in type II spiral ganglion neurons in vitro. *Neurosci. Lett.* **478**, 51–55. https://doi.org/10.1016/j.neulet.2010.01.063 (2010).
25. Barclay, M., Ryan, A. F. & Housley, G. D. Type I vs type II spiral ganglion neurons exhibit differential survival and neuritogenesis during cochlear development. *Neural Dev.* **6**, 33. https://doi.org/10.1186/1749-8104-6-33 (2011).
26. Huang, L. C., Thorne, P. R., Housley, G. D. & Montgomery, J. M. Spatiotemporal definition of neurite outgrowth, refinement and retraction in the developing mouse cochlea. *Development* **134**, 2925–2933. https://doi.org/10.1242/dev.001925 (2007).
27. Karpov, V., Landon, F., Djabali, K., Gros, F. & Portier, M. M. Structure of the mouse gene encoding Peripherin: a neuronal intermediate filament protein. *Biol. Cell.* **76**, 43–48. https://doi.org/10.1016/0248-4900(92)90193-5 (1992).
28. Belecky-Adams, T., Wight, D. C., Kopchick, J. J. & Parysek, L. M. Intragenic sequences are required for cell type-specific and injury-induced expression of the rat peripherin gene. *J. Neurosci.* **13**, 5056–5065. https://doi.org/10.1523/jneurosci.13-12-05056.1993 (1993).
29. Leconte, L. et al. Cell type-specific expression of the mouse peripherin gene requires both upstream and intragenic sequences in Transgenic mouse embryos. *Brain Res. Dev. Brain Res.* **92**, 1–9. https://doi.org/10.1016/0165-3806(95)00182-4 (1996).
30. Lariviere, R. C., Nguyen, M. D., Ribeiro-da-Silva, A. & Julien, J. P. Reduced number of unmyelinated sensory axons in peripherin null mice. *J. Neurochem.* **81**, 525–532. https://doi.org/10.1046/j.1471-4159.2002.00853.x (2002).
31. Uveges, T. E., Shan, Y., Kramer, B. E., Wight, D. C. & Parysek, L. M. Intron 1 is required for cell type-specific, but not injury-responsive, peripherin gene expression. *J. Neurosci.* **22**, 7959–7967. https://doi.org/10.1523/jneurosci.22-18-07959.2002 (2002).
32. Elliott, K. L., Kersigo, J., Pan, N., Jahan, I. & Fritzsch, B. Spiral ganglion neuron projection development to the hindbrain in mice lacking peripheral and/or central target differentiation. *Front. Neural Circuits.* **11** https://doi.org/10.3389/fncir.2017.00025 (2017).
33. Barclay, M., Noakes, P. G., Ryan, A. F., Julien, J. P. & Housley, G. D. Neuronal expression of peripherin, a type III intermediate filament protein, in the mouse hindbrain. *Histochem. Cell. Biol.* **128**, 541–550. https://doi.org/10.1007/s00418-007-0340-4 (2007).

34. Petitpré, C. et al. Single-cell RNA-sequencing analysis of the developing mouse inner ear identifies molecular logic of auditory neuron diversification. *Nat. Commun.* **13**, 3878. https://doi.org/10.1038/s41467-022-31580-1 (2022).
35. NHMRC. Australian code for the care and use of animals for scientific purposes. Australian Federal Government National Health and Medical Research Council 8th Edition, ISBN 1864965975. (2013).
36. Percie du Sert. Reporting animal research: explanation and elaboration for the ARRIVE guidelines 2.0. *PLoS Biol.* **18**, e3000411. https://doi.org/10.1371/journal.pbio.3000411 (2020).
37. Delerue, F. & Ittner, L. M. Generation of genetically modified mice through the microinjection of oocytes. *J. Vis. Exp.* https://doi.org/10.3791/55765 (2017).
38. Wick, R. R., Judd, L. M. & Holt, K. E. Performance of neural network basecalling tools for Oxford nanopore sequencing. *Genome Biol.* **20**, 129. https://doi.org/10.1186/s13059-019-1727-y (2019).
39. Smolka, M. et al. Comprehensive structural variant detection: from mosaic to population-level. *BioRxiv* **2022.2004.2004.487055** https://doi.org/10.1101/2022.04.04.487055 (2023).
40. Vaser, R. & Šikić, M. Time- and memory-efficient genome assembly with Raven. *Nat. Comput. Sci.* **1**, 332–336. https://doi.org/10.1038/s43588-021-00073-4 (2021).
41. Cabanettes, F. & Klopp, C. D-GENIES: Dot plot large genomes in an interactive, efficient and simple way. *PeerJ* **6**, e4958. https://doi.org/10.7717/peerj.4958 (2018).
42. Li, H. Minimap2: pairwise alignment for nucleotide sequences. *Bioinformatics* **34**, 3094–3100. https://doi.org/10.1093/bioinformatics/bty191 (2018).
43. Kolmogorov, M., Yuan, J., Lin, Y. & Pevzner, P. A. Assembly of long, error-prone reads using repeat graphs. *Nat. Biotechnol.* **37**, 540–546. https://doi.org/10.1038/s41587-019-0072-8 (2019).
44. Vaser, R., Sović, I., Nagarajan, N. & Šikić, M. Fast and accurate de Novo genome assembly from long uncorrected reads. *Genome Res.* **27**, 737–746. https://doi.org/10.1101/gr.214270.116 (2017).
45. Shumate, A. & Salzberg, S. L. Liftoff: accurate mapping of gene annotations. *Bioinformatics* **37**, 1639–1643. https://doi.org/10.1093/bioinformatics/btaa1016 (2021).
46. Mirdita, M. et al. ColabFold: making protein folding accessible to all. *Nat. Methods*. **19**, 679–682. https://doi.org/10.1038/s41592-022-01488-1 (2022).
47. Jing, D. et al. Tissue clearing of both hard and soft tissue organs with the PEGASOS method. *Cell Res.* **28**, 803–818. https://doi.org/10.1038/s41422-018-0049-z (2018).
48. Susaki, E. A. et al. Whole-Brain imaging with Single-Cell resolution using chemical cocktails and computational analysis. *Cell* **157**, 726–739. https://doi.org/10.1016/j.cell.2014.03.042 (2014).
49. Cederholm, J. M. et al. Differential actions of isoflurane and ketamine-based anaesthetics on cochlear function in the mouse. *Hear. Res.* **292**, 71–79. https://doi.org/10.1016/j.heares.2012.08.010 (2012).
50. Cederholm, J. M. E., Ryan, A. F. & Housley, G. D. Onset kinetics of noise-induced purinergic adaptation of the 'cochlear amplifier'. *Purinergic Signal.* **15**, 343–355. https://doi.org/10.1007/s11302-019-09648-3 (2019).
51. Jumper, J. et al. Highly accurate protein structure prediction with alphafold. *Nature* **596**, 583–589. https://doi.org/10.1038/s41586-021-03819-2 (2021).
52. Evans, R. et al. Protein complex prediction with AlphaFold-Multimer. *bioRxiv*, 2021.2010.2004.463034, (2022). https://doi.org/10.1101/2021.10.04.463034
53. Heffner, H. E. & Heffner, R. S. Hearing ranges of laboratory animals. *J. Am. Assoc. Lab. Anim. Sci.* **46**, 20–22 (2007).
54. Wong, Y. Y. et al. Parallel recovery of chromatin accessibility and gene expression dynamics from frozen human regulatory T cells. *Sci. Rep.* **13**, 5506. https://doi.org/10.1038/s41598-023-32256-6 (2023).
55. Girotto, G. et al. Expression and replication studies to identify new candidate genes involved in normal hearing function. *PLoS One*. **9**, e85352. https://doi.org/10.1371/journal.pone.0085352 (2014).
56. Sun, S., Siebald, C. & Müller, U. Subtype maturation of spiral ganglion neurons. *Curr. Opin. Otolaryngol. Head Neck Surg.* **29**, 391–399. https://doi.org/10.1097/moo.0000000000000748 (2021).
57. Niswender, C. M. & Conn, P. J. Metabotropic glutamate receptors: physiology, pharmacology, and disease. *Annu. Rev. Pharmacol. Toxicol.* **50**, 295–322. https://doi.org/10.1146/annurev.pharmtox.011008.145533 (2010).
58. Ingham, N. J. et al. Functional analysis of candidate genes from genome-wide association studies of hearing. *Hear. Res.* **387**, 107879. https://doi.org/10.1016/j.heares.2019.107879 (2020).
59. Zhang, D. et al. Lypd1-DTR/+: A new mouse model for specifically damaging the type Ic spiral ganglion neurons of the cochlea. *Neurosci. Bull.* **39**, 1459–1462. https://doi.org/10.1007/s12264-023-01071-4 (2023).
60. Sherrill, H. E. et al. Pou4f1 defines a subgroup of type I spiral ganglion neurons and is necessary for normal inner hair cell presynaptic Ca(2+) signaling. *J. Neurosci.* **39**, 5284–5298. https://doi.org/10.1523/jneurosci.2728-18.2019 (2019).
61. Gong, S. et al. A gene expression atlas of the central nervous system based on bacterial artificial chromosomes. *Nature* **425**, 917–925. https://doi.org/10.1038/nature02033 (2003).
62. McLenachan, S. et al. Transgenic mice expressing the Peripherin-EGFP genomic reporter display intrinsic peripheral nervous system fluorescence. *Transgenic Res.* **17**, 1103–1116. https://doi.org/10.1007/s11248-008-9210-7 (2008).
63. Ruben, R. J. Development of the inner ear of the mouse: a radioautographic study of terminal mitoses. *Acta Otolaryngol. Suppl.* **220**, 221–244 (1967).
64. Rubel, E. W. & Fritzsch, B. Auditory system development: primary auditory neurons and their targets. *Annu. Rev. Neurosci.* **25**, 51–101. https://doi.org/10.1146/annurev.neuro.25.112701.142849 (2002).
65. Fritzsch, B., Pan, N., Jahan, I. & Elliott, K. L. Inner ear development: Building a spiral ganglion and an organ of Corti out of unspecified ectoderm. *Cell. Tissue Res.* **361**, 7–24. https://doi.org/10.1007/s00441-014-2031-5 (2015).
66. Greenwood, D. et al. P2X receptor signaling inhibits BDNF-mediated spiral ganglion neuron development in the neonatal rat cochlea. *Development* **134**, 1407–1417. https://doi.org/10.1242/dev.002279 (2007).
67. Wang, T. et al. Uncoordinated maturation of developing and regenerating postnatal mammalian vestibular hair cells. *PLoS Biol.* **17**, e3000326. https://doi.org/10.1371/journal.pbio.3000326 (2019).

Acknowledgements

We would like to acknowledge the Katerina Gaus Light Microscopy Facility as a part of the Mark Wainright analytical center for providing access to the Lightsheet microscope. The Garvan Institute for access to PromethION (ONT) Nanopore sequencing. The Ramaciotti Center for Genomics, especially Tonia Russell, for validating the DNA content and clean-up protocol for nanopore sequencing. We would also like to thank Sreya Santhakumar and Elena Venuti for supporting the studies.

Author contributions

Author contributions: LJP carried out experiments, analyzed data, collated figures, and wrote the manuscript alongside GDH, JMEC and GVJ. JLP and GDH conceptualized this mouse model design, with FD and LMI producing the mouse lines. FB conceptualized the visualization protocol for Lightsheet imaging. XVC processed

bioinformatics data for the integration site and AlphaFold analysis. JMEC led the hearing testing experiments. All authors reviewed the manuscript.

Funding
The studies were supported by the Australian National Health and Medical Research Council (NHMRC) grant refs. APP1189113 & APP1188643.

Declarations

Animal ethics statement
The study protocol was approved by the UNSW Animal Care and Ethics Committee and followed the National Health and Medical Research Council (NHMRC) guidelines for the care and use of animals for laboratory-based research.

Competing interests
The authors declare no competing interests.

Additional information
Supplementary Information The online version contains supplementary material available at https://doi.org/10.1038/s41598-025-94011-3.

Correspondence and requests for materials should be addressed to G.D.H.

Reprints and permissions information is available at www.nature.com/reprints.

Publisher's note Springer Nature remains neutral with regard to jurisdictional claims in published maps and institutional affiliations.